

Non-Invasive Measurement Methods for Transient Flows in Wind Tunnels

by

Joseph P. Marcheggiani

A Thesis Submitted to the Faculty of the

College of Engineering and Computer Science

In Partial Fulfillment of the Requirements for the Degree of

Master of Science

Florida Atlantic University

Boca Raton, FL

December 2021

Copyright 2021 by Joseph P. Marcheggiani

Non-Invasive Measurement Methods for Transient Flows in Wind Tunnels

by

Joseph P. Marcheggiani

This thesis was prepared under the direction of the candidate's thesis advisor, Dr. Stewart Glegg, Department of Ocean and Mechanical Engineering, and has been approved by all members of the supervisory committee. It was submitted to the faculty of the College of Engineering and Computer Science and was accepted in partial fulfillment of the requirements for the degree of Master of Science.


SUPERVISORY COMMITTEE:



Stewart Glegg, Ph.D.
Thesis Advisor


Aditya R Nayak (Nov 22, 2021 22:19 EST)

Aditya Nayak, Ph.D.


Siddhartha Verma (Nov 24, 2021 11:57 EST)

Siddhartha Verma, Ph.D.



Manhar Dhanak, Ph.D.
Chair, Department of Ocean and
Mechanical Engineering



Stella Batalama, Ph.D.
Dean, College of Engineering and
Computer Science



Robert W. Stackman Jr., Ph.D.
Dean, Graduate College

November 29, 2021

Date

Acknowledgements

I would like to sincerely thank my thesis advisor, Dr. Stewart Glegg, for giving me the opportunity to partake in this coveted research. I am so grateful for his guidance and support throughout this astounding educational experience. I am honored to have worked alongside someone with such expertise in engineering and knowledge in fluid dynamics and acoustics. I cannot express my gratitude enough for his tremendous patience conducting research virtually during these unprecedented times. I would like to thank Dr. Aditya Nayak and Dr. Siddhartha Verma for being part of my committee and providing me with valuable feedback. I wish to thank the Office of Naval Research for the support of this study under the research grant N00014-20-1-2665.

I wish to express my gratitude to my family, who has supported me every step of the way and for always believing in me. I could not have made it nearly this far without their unconditional love and support throughout my life. Finally, I would like to thank my grandfather Joseph Marcheggiani for motivating me to continue my education and advancing my career as an engineer.

Joseph P. Marcheggiani

Abstract

Author: Joseph P. Marcheggiani
Title: Non-Invasive Measurement Methods for Transient Flows in Wind Tunnels
Institution: Florida Atlantic University
Thesis Advisor: Dr. Stewart Glegg
Degree: Master of Science
Year: 2021

A non-invasive transient state measurement method for wind tunnels would be very valuable as an experimental tool. Traditional measurement techniques for transient flows, e.g., hot wire anemometry, require sensors that are placed in the flow. Alternatively, particle image velocimetry (PIV) may be used to measure transient flows non intrusively, but applying PIV requires sensors that are expensive, and it may take months to process the data. The non-invasive measurement techniques considered in this thesis utilize sensors that are imbedded into the wall of a wind tunnel, or the response of a Kevlar walled wind tunnel to obtain the pressure time histories of a transient flow. These measurements are suitable and accurate for analyzing steady state flows but the feasibility of using them on time varying flows has yet to be explored. If this method proves possible, it would be very beneficial even if it is less accurate than current invasive methods because it would give results in real time. This thesis investigates a simple

transient flow of the startup vortex of an airfoil caused by a step change in angle of attack. Based on thin airfoil theory, two models of an airfoil were created. It was determined that the response of a Kevlar wall can measure the unsteady lift of an airfoil.

Non-Invasive Measurement Methods for Transient Flows in Wind Tunnels

List of Figures	x
Table of Symbols	xii
Chapter 1: Introduction	1
Chapter 2: Literature Review	3
2.1 Wind Tunnels, Sensors and Measurement Methods	3
2.2 Relevant work	6
2.3 Relevant Fluid Dynamic Concepts	17
2.4 Starting Vortex	19
Chapter 3: The Simple Vortex Model	22
3.1 Approach	22
3.1.1 The Simple Vortex Model	22
3.1.2 Vortices, Image Vortices and Wall Boundary Conditions	23
3.1.3 Lift Force, Wagner's Function, and Circulation	32
3.1.4 Time Less Than the Critical Time	35
3.1.5 Time Greater Than the Critical Time	37
3.1.6 Convection Acceleration	39

3.2 Wall Pressure Measurements	41
3.2.1 Wall Pressure Calculation	41
3.2.2 Coefficient of Pressure	41
3.2.3 Pressure Spectrum and Goody Model	41
3.2.4 Noise Estimates and Removal	43
3.3 Simple Vortex Model Results	44
3.3.1 Pressure Time History	44
3.3.2 Pressure Time History for Various Convection Acceleration Time Periods	48
3.3.3 Spectral Analysis and Filtering	51
3.4 Simple Vortex Model Conclusions	54
Chapter 4. Vortex Sheet Model and Kevlar Membrane Response	56
4.1 Approach	56
4.1.1 Vortex Sheet Model	56
4.1.2 Pressure Calculation	57
4.1.3 Membrane Response	62
.....	67
4.2 Sheet Vortex Model and Kevlar Membrane Results	67
4.3 Sheet Vortex Model and Kevlar Membrane Conclusions	70
Chapter 5: Discussion	72

5.1 Simple Vortex Model.....	72
5.2 Vortex Sheet Model and Kevlar Wall Response	75
Chapter 6: Conclusion.....	76
6.1 Conclusion	76
6.2 Recommendations.....	78
Chapter 7: Appendix	80
7.1 Additional Information on Kenneth Brown's Work.....	80
Chapter 8: References	83

List of Figures

Figure 1: Schematic of Control Volume Region of The Kevlar Walled Test Section [4].	8
Figure 2: Experimental Configuration of The Test Section at The Aeroacoustic Virginia Tech Stability Wind Tunnel [4].	11
Figure 3: Raw Displacement of Kevlar Wall Results [4].	13
Figure 4: Wall Pressure Distributions Results [4].	14
Figure 5: a-c Optically inferred C_p distributions compared with pressure tap measurements for angles of attack 0, 7.8 and 14.7 degrees. d integrated C_l values vs angle of attack compared with pressure tap measurements [4].	16
Figure 6: Starting vortex of an Airfoil [8].	20
Figure 7: Airfoil Simple Vortex Model.	22
Figure 8: Streamlines of a Vortex in Free Space.	24
Figure 9: Streamlines of a Vortex with One Image Vortex.	25
Figure 10: Vertical Component of Velocity Along the Non-Penetration Boundary.	26
Figure 11: Two Image Vortices.	27
Figure 12: Vertical Component of Velocity Along the Non-Penetration Boundary.	28
Figure 13: Summation of Image Vortices.	30
Figure 14: Vertical Velocity Component Along the Non-Penetration Boundary 1 and 2.	31
Figure 15: Wagner Function Response.	34

Figure 16: Simple Vortex Model Material Contour.	35
Figure 17: Airfoil Simple Vortex Model Time Greater Than Critical Time.	38
Figure 18: The pressure time history for a transducer located in the wind tunnel wall at the mid chord point.	45
Figure 19: The pressure time history for a transducer located in the wind tunnel wall at 1 chord length downstream.	46
Figure 20: The pressure time history for a transducer located in the wind tunnel wall at 3 chord lengths downstream.	47
Figure 21: wall pressure signal taken at the mid chord for six different convection acceleration periods	49
Figure 22: Wall pressure signal taken one chord length downstream for six different convection acceleration periods.	50
Figure 23: Wall pressure signal taken 3 chord lengths downstream for six different convection acceleration periods.	51
Figure 24: Spectral Analysis of Signal located 3 Chord Lengths Downstream With T=30 and the Estimated Amount of Background Noise.	53
Figure 25: Spectral Analysis of Signal located 3 Chord Lengths Downstream With T=30 and 10 Times the Estimated Amount of Background Noise.	54
Figure 26: Vortex Sheet Model.....	57
Figure 27: Kevlar Membrane Displacement at The Trailing Edge.....	68
Figure 28: Kevlar Membrane Response at The Trailing Edge for Various Tension	69
Figure 29: Kevlar Membrane Response at The Trailing Edge for Various Flow Speeds	70

Table of Symbols

u, v, w	Regularized displacement in x direction
Δp	Pressure difference across membrane
$p_{chamber}$	Static pressure inside anechoic chamber
$T_{x,\varepsilon}, T_{y,\varepsilon}, T_{xy,\varepsilon}$	Strain induced tensions
$T_{x,0}, T_{y,0}, T_{xy,0}$	Pre-tensions
$\varepsilon_x, \varepsilon_y, \gamma_{xy}$	Strain displacement relationship
T	Tension
E	Elastic moduli
G	Shear modulus
V	Poisson's ratio
c	Chord Length
C_p	Coefficient of pressure
C_l	Coefficient of lift
$\frac{\partial u}{\partial x'}, \frac{\partial v}{\partial y'}$	Load-induced loss in pre-tension
V_∞	Free stream velocity
ρ_∞	Free steam density
p_∞	Free stream pressure
H	Fabric thickness
$w(z)$	Complex potential
$w'(z)$	Complex velocity
x_m	X location of observer
z	Observer location
z_n	Shed vortex center
z_c	Bound vortex center

Γ	Circulation
H	Distance from wall
q	Dynamic pressure
α	Angle of attack
N	Constant for number of image vortices
n	Ranges from -N:N
b	Non dimensional reference length
w_o	Step gust
U_∞	Free stream velocity
ρ	Fluid density
L	Unsteady Lift
$\varphi(t^*)$	The Wagner Function
t	Time
t^*	Non dimensional time
t_c^*	Critical time
τ	Time after critical time
T	Convection acceleration period
Γ_o	Airfoil Circulation
Γ_n	Circulation
x_n	X location of the center of the shed vortex
U_c	Steady state convection velocity
$u(t)$	Unsteady convection velocity
G_{pp}	Wall pressure spectrum
C_1, C_2, C_3	Goody constants
ω	Frequency
δ	Boundary layer thickness
U_e	Edge velocity
u_τ	Inner velocity
R_T	Ratio of outer and inner layer timescales
C_{Prms}	Non dimensional RMS pressure

G	Array of standard normal distribution
ζ	Position of vortex sheet
x_o	Location of vortex representing the airfoil
Γ_{max}	Max airfoil circulation
L_{max}	Max lift
$H(t)$	Heaviside function
x'	Membrane x coordinate
y'	Membrane y coordinate
c_t	Speed of wave in a membrane
ρ_a	Mass per unit area
z	Membrane surface displacement
L_x	Length of membrane in x direction
L_y	Length of membrane in y direction

Chapter 1: Introduction

Non-invasive transient state measurement methods for wind tunnels would be very valuable as an experimental tool. Traditional measurement techniques for transient flows require sensors that are placed in the flow, for example a hot wire anemometer or PIV set up [1]. These measurement techniques can accurately measure velocities of a fluid flow but applying these sensors are expensive and it may take months to process the data. Kevlar walled wind tunnel measurement techniques have been explored by Bahr [2], Szoke [3] and Mayer [4]. The non-invasive measurement techniques considered in this thesis utilize sensors that are imbedded into the wall of a wind tunnel, or the response of a Kevlar walled wind tunnel to track the wake of a transient flow. These two measurements techniques are suitable and accurate for analyzing steady state flows but the feasibility of using them on time varying flows has yet to be explored. If either of these two methods proves experimentally viable, it would allow transient state measurements to be done in one shot, giving instantaneous results [1]. This non-invasive technique would be very beneficial even if it is less accurate than current invasive methods because it would give results in real time. To evaluate the feasibility of non-invasive measurement techniques on transient flows, two models have been developed to analyze a simple transient flow based on the startup vortex of an airfoil caused by a step change in angle of attack that's described by the Wagner function.

The first model describes the airfoil as an equal and opposite vortex according to Kelvin's theorem. It is assumed that the airfoil operates with low drag and the boundary

layer is thin relative to the thickness of the airfoil, so the boundary layer can be ignored. Furthermore, the flow is assumed to be homentropic, incompressible and of low Mach number, so that the governing equations become more manageable. Considering the flow to be ideal reduces the momentum equation to Bernoulli's equation which is then used to calculate the pressure field. Furthermore, the continuity equation simplifies to Laplace's Equation and a solution to the Laplace's Equation, in two dimensions, can be any analytic function of a complex variable. This is very convenient for modeling the velocity field of a vortex, and the complex potential, streamlines and velocity field is easily found [1]. The boundary conditions at the walls of the wind tunnel are satisfied by the method of image vortices. For the case of the startup vortex a critical time is defined which is when the trailing edge vortex grows to its maximum intensity, separates, and begins to convect downstream. For time less than the critical time the strength of the starting vortex is a function of time. However, once the vortex separates from the trailing edge its strength remains constant, in principle, but its convection speed varies. When the startup vortex is separating from the trailing edge both its strength and position could be a function of time. The Wagner function is used to estimate the critical time and equations of motion are developed to describe the time series of these vortices. As a result, the wall pressure time history of these vortices is found.

The second model uses thin airfoil theory and assumes the airfoil to be a flat plate that is infinitely thin. Using the approach set forth by Newman, the flow field of the flat plate is described as vortex sheet. This led to more manageable equation that could obtain the membrane response through Laplace transforms.

Chapter 2: Literature Review

2.1 Wind Tunnels, Sensors and Measurement Methods

Wind tunnels have been used as the principal means of testing in experimental aerodynamics for over a century. In the 1960's, computational fluid dynamics methods were developed, and it was hoped that computational methods would become the method of choice and that the wind tunnel would eventually not be needed [2]. However, today, wind tunnels continue to be the main tool for experimental aerodynamics and improved technology has led to new wind tunnels configurations. Currently, theoretical and computational techniques still serve an important role in experimental aerodynamics, and the best approach to an aerodynamic design problem is to incorporate the results of theoretical and computational methods with the results obtained from wind tunnel experiments [2].

Experimental aerodynamic testing is typically carried out in a wind tunnel due to the low costs relative to conducting a field test. Additionally, a wind tunnel offers an isolated environment where the properties of the flow can be precisely controlled, and the results of experiments are repeatable. Control over the Reynolds number, Mach number and Froude number is essential to achieve flow similarity when using a scaled model [2]. These similarity parameters are dimensionless numbers that are ratios of internal, viscous and gravitational forces and in this case, they are used to determine the flow similarity between a scale model and full-sized model [2]. If the flow over the scaled model and the

full-sized model have the same similarity parameters then the relevant importance of the forces are correctly modeled and the flows will be dynamically similar [2] [3]. Wind tunnels are designed to have as little aerodynamic interference as possible so that the modeled flow is close to the desired flow. To account for any discrepancy between the modeled and desired flow, interference corrections are used [1]. It is desirable for a wind tunnel to operate with a small interference correction so that higher Reynolds numbers can be reached [1].

There are many variations of wind tunnels that exist today all of which are derived from two basic families defined as open circuit and closed circuit systems. There are also two main types of test section that a wind tunnel can have, defined as an open or closed test section. Many wind tunnels are unique and use a hybrid test section that is a combination of a closed and open test section [2]. Aeroacoustic wind tunnels are a variety of wind tunnel that focuses on measuring the noise produced by a model subjected to a fluid flow. Military applications, such as categorizing and reducing flow generated noise from submarines, and civilian applications, such as categorizing and reducing flow generated noise from aircraft, have driven the development of this kind of wind tunnel [2]. Aeroacoustic wind tunnels are designed similar to a closed circuit wind tunnel but the equipment such as ducts, fans and turning vanes, are engineered to produce as little noise as possible during operation [2]. Additionally, one or more mufflers are attached in series with the ducts to minimize background noise [2]. Furthermore, aeroacoustic wind tunnels offer a method of taking far field sound measurements with the use of an anechoic chamber and microphone array [1]. An open test section may be used so that the flow passes through the anechoic chamber as a jet, such as NASA's Quiet Flow Facility, or a

closed test section may be used so that the flow is contained by walls with acoustically transparent windows, such as the Anechoic Flow Facility at the Naval Surface Warfare Center (NSWC) Carderock Division [1]. Acoustically transparent windows are typically made from a Kevlar weave due to its high acoustic transparency and its strength that can contain the fluid flow [1].

Pressure transducers are the typical sensor used in wind tunnels as a means to measure pressure. These sensors are used to measure pressure fluctuation in the initial flow, on the surface of the model and along the walls of the test section. A traditional pressure transducer utilizes a diaphragm that deforms with changes in pressure along its surface [2]. This deformation is then measured by either a strain gauge, an electric circuit that measure change in capacitance or the change in inductance, depending on the type of pressure transducer [2]. It is important to consider the frequency of the pressure fluctuations of interest before selecting a model so that a pressure transducer with a sufficient dynamic range is selected.

A hot wire anemometer is a sensor typically used to measure unsteady velocities of a fluid flow inside a wind tunnel. This sensor utilizes a tiny metal wire, as small as 2.5 micrometers in diameter, that is heated to a known temperature by the current of an electric circuit [1]. Since the wire is maintained at a constant temperature and the resistance does not change only the voltage is varied. The variation in voltage is then related to the velocity of the passing fluid so that the velocity at a single point is obtained [1]. The signal from a hot wire varies in time so the velocity spectra is easily obtained if needed [1]. Furthermore, space time correlations can be determined if multiple sensors are used [1]

There are various experiments that can be carried out in a wind tunnel. Steady state wind tunnel experiments utilize a flow with constant velocity that passes over the test model with a set angle of attack. This flow is then analyzed by sensors that can be imbedded on the surface of the model or along the walls of the tunnel. These sensors collect data on the flow both inside and outside of the boundary layer and the flow can be categorized. Transient state wind tunnel experiments typically vary the angle of attack of the test model so that the flow becomes dependent on time. Traditional measurement techniques for transient flow measurements require sensors that are placed in the flow to measure fluid velocities, for example a hot wire [1]. These measurement techniques can accurately measure velocities of the fluid flow although running these sensors are expensive and may take months to process the data. Additionally, these measurement techniques are invasive as they obstruct the flow and cause unwanted fluid dynamic interactions that skew pressure and acoustic measurements. To avoid these unwanted interactions, multiple runs of the same experiment must be conducted so that these parameters can be measured separately however this increases the time and cost of the experiment [1].

2.2 Relevant work

The work by Brown et al. [4] proposed a novel non-invasive measurement method for aerodynamics in a wind tunnel. Brown's work focused on steady state measurements taken specifically in Kevlar walled test sections, but the feasibility of using this method for transient state measurements has yet to be determined. The following section is a review of the work done by Brown et al. [4]

Kevlar walled aeroacoustic wind tunnels, such as the Aeroacoustic Virginia Tech Stability Wind Tunnel, allow for simultaneous aeroacoustic and aerodynamic measurements. Kevlar cloth is acoustically transparent and when it is placed under tension as a wind tunnel wall it can contain the flow within the wind tunnel test section. Acoustic equipment, such as microphone arrays, can then be placed behind the Kevlar wall and shielded from the flow where far field acoustic measurements are made. However, the Kevlar walled test sections also hinders the ability to take certain aerodynamic measurements [4] such as wall pressure measurements. Wall pressures, along with a control volume analysis can be used as an alternative, non-invasive method to calculate the lift of a model [4]. Wall interference corrections are also determined with wall pressure data when the linear theory for these corrections is inadequate [4]. Brown et al [4] attempted to take wall pressure measurements in a Kevlar walled test section using pressure taps on the anechoic side of the Kevlar wall [5]. Unfortunately, there was leakage around these pressure taps and some even became dislodged, ultimately proving this method inadequate for a primary tool of measuring wall pressures [5]. Brown et al. [4] then used the Kevlar itself to measure the pressure along the wall. Figure 1 shows a schematic of the control volume region of the Kevlar walled test section. Brown et al. [4] assumed a steady-state, incompressible and two-dimensional flow.

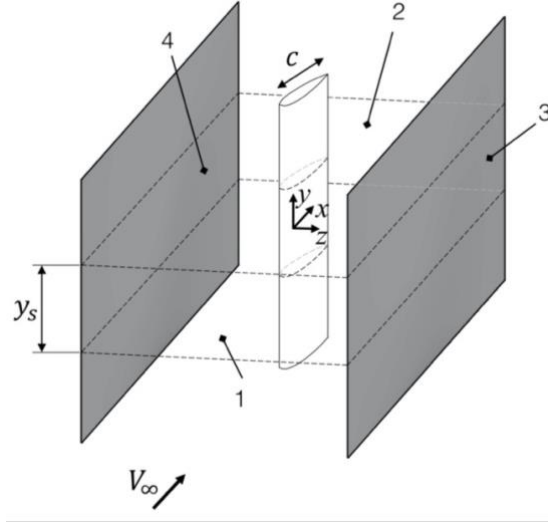


Figure 1: Schematic of Control Volume Region of The Kevlar Walled Test Section [4].

Brown et al. [4] carried out theoretical calculations by relating the loads on one side of the Kevlar wall to the derivative of the displacement field on the opposite side. This provides an equation for the pressure difference across the membrane as

$$\Delta p = (T_{x,\varepsilon} + T_{x,0}) \frac{\partial^2 w}{\partial x^2} + (T_{y,\varepsilon} + T_{y,0}) \frac{\partial^2 w}{\partial y^2} + 2(T_{xy,\varepsilon} + T_{xy,0}) \frac{\partial^2 w}{\partial x \partial y} \quad (1)$$

where Δp is the pressure jump, T are tensions, w are the wall displacements and x, y are the locations on the wall. The subscript 0 denotes the pre-tensions and the subscript ε represents strain induced tensions. Substituting the strain displacement and stress strain relationships for the Kevlar membrane into Equation (1) yields the equation for the pressure displacement across the membrane, as

$$\Delta p = \left\{ \frac{E_x h \left[\frac{\partial u}{\partial x} + \frac{1}{2} \left(\frac{\partial w}{\partial x} \right)^2 + v_{yx} \left(\frac{\partial v}{\partial y} + \frac{1}{2} \left(\frac{\partial w}{\partial y} \right)^2 \right) \right]}{1 - v_{xy} v_{yx}} + T_{x,0} \right\} \frac{\partial^2 w}{\partial x^2} + \left\{ \frac{E_y h \left[\frac{\partial v}{\partial y} + \frac{1}{2} \left(\frac{\partial w}{\partial y} \right)^2 + v_{xy} \left(\frac{\partial u}{\partial x} + \frac{1}{2} \left(\frac{\partial w}{\partial x} \right)^2 \right) \right]}{1 - v_{xy} v_{yx}} + T_{y,0} \right\} \frac{\partial^2 w}{\partial y^2} \quad (2)$$

where E_x , E_y and v_{xy} are nonlinear material properties of the Kevlar fabric. Assuming an effective thickness of $H = 0.0210$ - mm, the material properties of the 120-style, plain-woven Kevlar fabric were determined to be $E_x = 1.33\text{e}10\text{-Pa}$, $E_y = 3.12\text{e}10\text{-Pa}$, and $v_{xy} = 0.40$,

To evaluate this equation the displacements in three dimensions are fitted with the basis functions, shown in the appendix, and then used in Equation (2) to provide a direct calculation of Δp [4]. The static pressure is measured inside the chamber so that the absolute pressure against the Kevlar wall is known. It is noted that the shear terms have been omitted because the shear modulus is very small, and its effects are insignificant [4]. Also, any load-induced loss in pre-tension due to imperfect boundary conditions where the Kevlar is pinned is accounted for with the addition of terms $\frac{\partial u}{\partial x}$ and $\frac{\partial v}{\partial y}$ [4].

The two-dimensional lift coefficient C_l , which represents the lift force per unit span and can be calculated as a function of the test section wall pressure Δp and the fluid exchange across boundaries 1, 2, 3 and 4 in figure 1 [4]. Using a control volume analysis of the flow within the Kevlar walled test section the continuity of momentum gives [4].

$$C_l = \frac{1}{c} \left[\int_{x_1}^{x_2} (C_{p,4} - C_{p,3}) dx + \int_{z_3}^{z_4} \frac{(w_1 u_1 - w_2 u_2)}{\frac{1}{2} V_\infty^2} dz + \int_{x_1}^{x_2} \frac{(w_4^2 - w_3^2)}{\frac{1}{2} V_\infty^2} dx \right] \quad (3)$$

Where the subscripts denote the location and the coefficient of pressure C_p is defined as

$$C_p = \frac{p_{chamber} \pm \Delta p - p_\infty}{\frac{1}{2} \rho_\infty V_\infty^2} \quad (4)$$

The values for C_l were compared with two independent measurement techniques to confirm the accuracy of this measurement method [4].

Brown et al. [4] carried out experiments in the Aeroacoustic Virginia Tech Stability Wind Tunnel. The experimental set up, shown in figure 2, consisted of two Kevlar membranes that ran from the floor to the ceiling and the length of the port and starboard walls of the test section. The Kevlar membranes were held in place by a metal frame and tension was applied to the in horizontal and vertical directions by rollers on the edge of the frame. Tension measurements were made at multiple locations to determine the mean pre-tensions. Anechoic chambers located on the opposite side of each Kevlar membrane are sealed so that the static pressure inside each chamber is a function of wind loading [4]. A three-dimensional digital image correlation (3D-DIC) system was used inside each of the anechoic chambers to measure the displacement of the Kevlar membranes. A specialized speckled coating that glows green in the presence of UV light was applied to each Kevlar membrane. The cameras of the 3D-DIC system tracked these

green speckles to determine the displacement of the walls. The floor and ceiling of the test section were made from aluminum plates and a NACA0012 airfoil was positioned vertically in the middle of the test section. The angle of attack of the airfoil was precisely controlled by a bearing and turntable system. Additionally, pressure taps were placed within the surface of the airfoil to measure lift and temporary pressure taps were installed in the Kevlar membrane itself to serve as an independent method of obtaining wall pressure measurements [4].

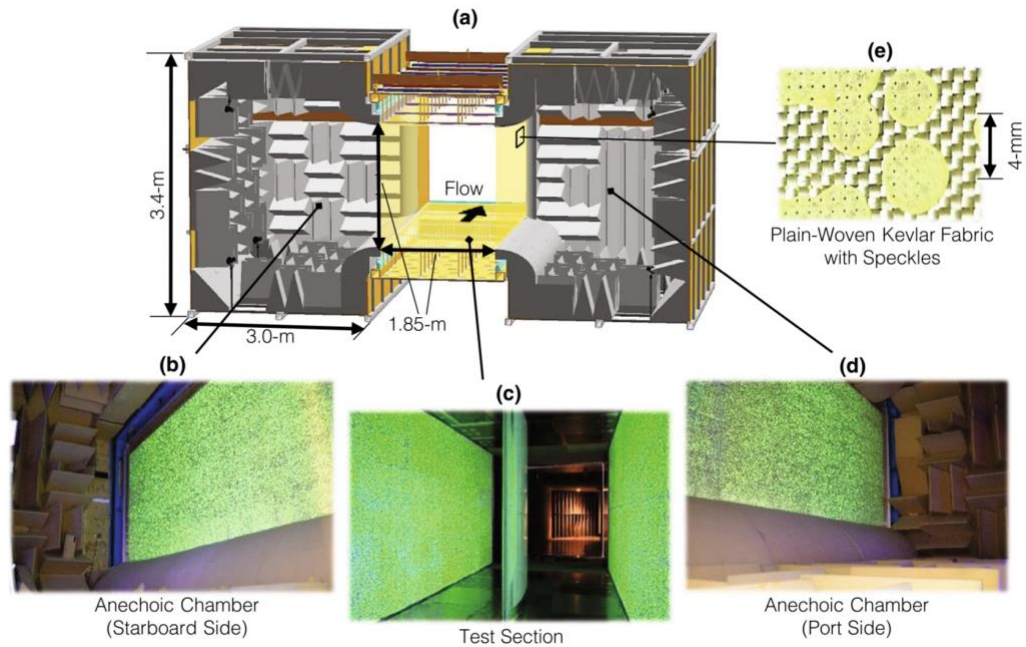


Figure 2: Experimental Configuration of The Test Section at The Aeroacoustic Virginia Tech Stability Wind Tunnel [4].

Determining a load from deflection, specifically calculating the pressure along a Kevlar wall from its displacement, creates an inverse problem. It requires a derivative of the displacement field and any errors that are contained in the displacement data set dramatically increase the error in its derivative. Therefore, it becomes important to obtain

accurate wall deformation measurements and minimize any uncertainties in the measurement method. To minimize uncertainties in the 3D-DIC system, Brown et al. [4] ensured that the cameras were focused sufficiently further than their hyperfocal lengths so that the Kevlar membranes stayed within the depth-of-vision during the duration of the experiments. Additionally, the cameras in the 3D-DIC system utilized a long exposure time. Brown et al. [4] limited the flow regime to steady state because the induced shape of the displacement of the Kevlar wall is relatively constant and the uncertainty in the measurement is low. On the other hand, transient flows, such as flow separations caused by large angles of attacks, produce dynamic displacements in the Kevlar wall that correspond to vortex shedding so that shape of the displacement is a function of time. Furthermore, an estimated displacement uncertainty of $\pm 40 - 60 \mu\text{m}$ is due to calibration and feature-matching errors [4]. Another source of uncertainty comes from tiny movements of the camera due to high freestream dynamic pressures. Fortunately, this type of uncertainty is minimum at low freestream dynamic pressures which were the focus of Brown's et al. [4] work.

The results for the Kevlar wall displacement measurements, shown in figure 3 as a contour plot, are from a flow with a freestream dynamic pressure of 770 Pa, a Reynolds number of 2×10^6 , a Mach number of 0.11 and an angle of attack of 7.8 degrees. These results use the raw data without corrections for wall interference. The displacement in the u and v plane are two orders of magnitude less than the magnitude of the displacement in the w plane. The vertical bands shown in figure 3a are a result of the interference caused by wall-mounted pressure taps [4]. Figure 3b shows the v displacements and how the Kevlar deformed away from the origin and at extreme values of y the displacement

changed directions. This is due to the roller frame bending inwards from holding the Kevlar wall under tension [4]. The w displacements are as expected and shows that the largest displacement is in the center of the Kevlar wall [4].

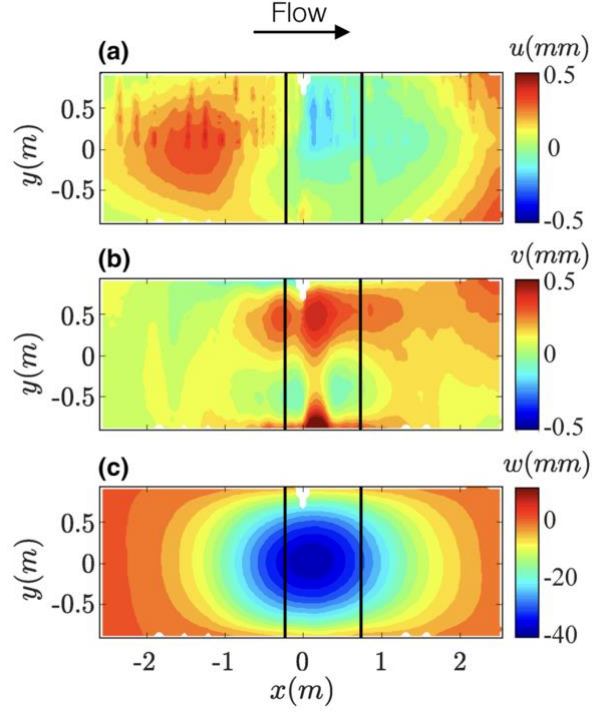


Figure 3: Raw Displacement of Kevlar Wall Results [4].

Brown et al. [4] regularized the displacement data with the techniques described in the appendix. The regularized data was used to compute the terms in equation 1 and then in equation 2 to compute C_p . The results for the non-shear terms and C_p are shown in figure 4 as contour plots. In figure 4a and b, the largest magnitude of stresses are located at the edges and corners. This is a result of bending in the roller frame due to the tension of the Kevlar membrane [4]. It can be seen that the pre-tensions shown in figures 4a and b are larger than the tensions induced by the flow shown in figures 4c and d.

Additionally, figure 4c and d show that the maximum strain induced tension has moved away from $y=0$, possibly from the inherent uncertainties of the Kevlar's material properties [4]. Figure 4e and 4f show a maximum along $y=0$ that correspond to the w displacement shown in figure 3c. Figure 4g shows the C_p extremum is shifted above $y=0$ similar to the trend of the T_ϵ plots [4]. Otherwise, the results for C_p are realistic for the suction-side of the Kevlar wall and show smooth variations [4].

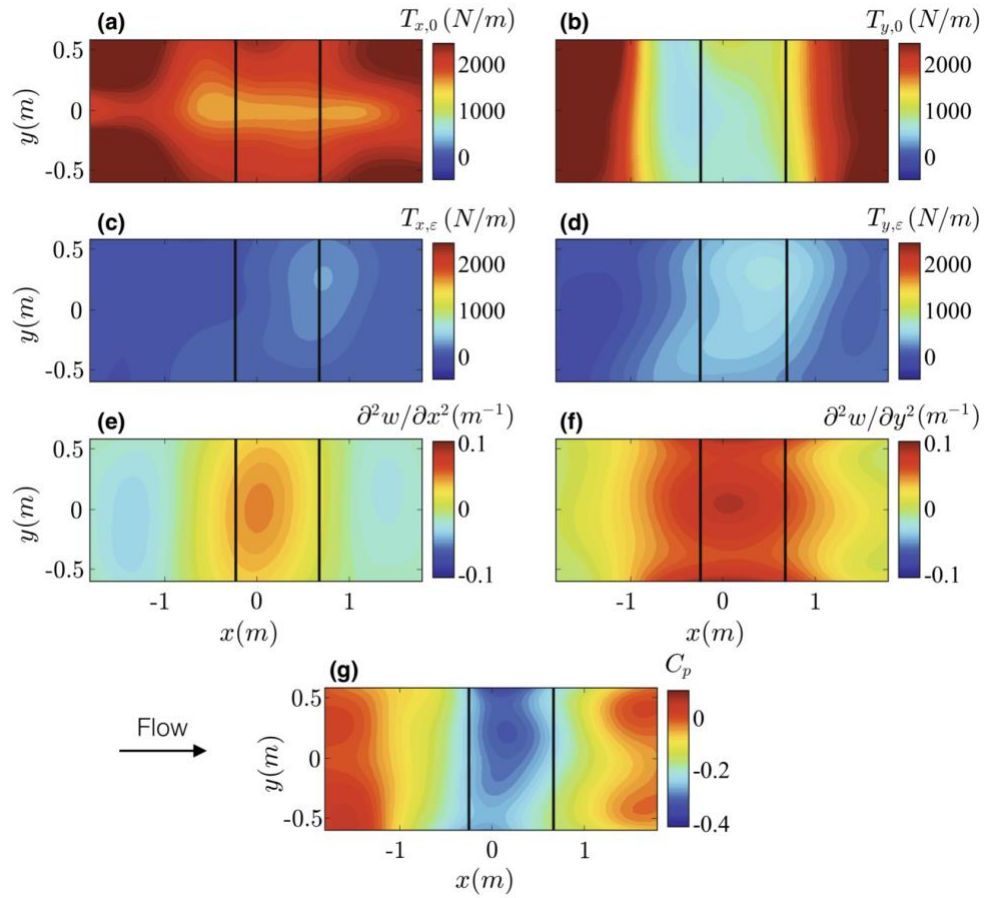


Figure 4: Wall Pressure Distributions Results [4].

To validate the results, Brown et al. [4] compared midspan C_p values with independent wall pressure measurements. The midspan C_p values were taken as the spanwise-average of the C_p values obtained by equation 4 within $y = \pm 0.3\text{m}$ of the midspan and the independent wall pressure measurements were obtained from pressure taps that were temporarily installed midspan in the Kevlar wall [4]. The C_p values for both Brown's et al. [4] method and the independent method were taken simultaneously. The C_p for values for both methods, shown in figure 5 a, b and c, have the same general shape. There are some discrepancies between the results on the suction side as the peaks are offset from one another [4]. Brown et al. [4] stated that this was due to either the spanwise averaging of the C_p values from the optical method or the effects of the uncertainty in the material properties of the Kevlar. Figure 5d shows the C_l values obtained by equation 3 vs the C_l values obtained by integrating data from pressure taps imbedded into the airfoil and Kevlar walls. All three measurement techniques follow the same trend up to a 7 degree angle of attack. At larger angles of attack, Brown et al.'s [4] optical method begins to show a different trend compared to the data obtained from the airfoil and wall mounted pressure taps. This suggests that Brown et al.'s [4] method becomes less accurate for larger values of lift due to systematic errors in measuring pretensions at the larger wall deflections and the uncertainties in the material properties of the Kevlar. The largest difference in the coefficient of lift between Brown et al.'s [4] method and the pressure taps imbedded in the airfoil was 5.4% [4]. The largest difference in C_l is determined for values only before the stall region as the accuracy of airfoil pressure taps deteriorates after stall. Due to uncertainties in measuring the Kevlar's pre-

tensions and uncertainties in the material properties, the estimated uncertainty for Brown et al.'s [4] method is larger than that of traditional pressure tap methods.

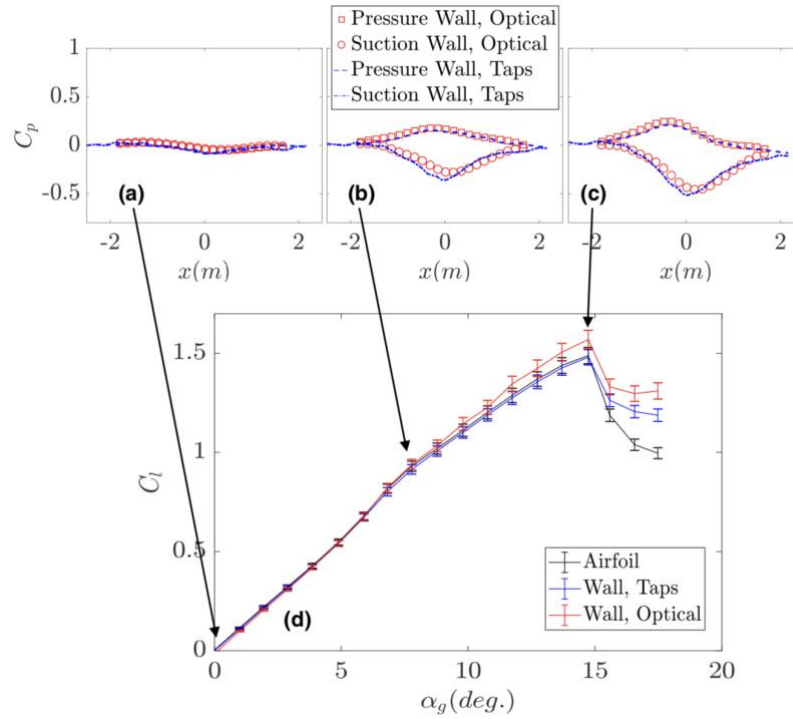


Figure 5: a-c Optically inferred C_p distributions compared with pressure tap measurements for angles of attack 0, 7.8 and 14.7 degrees. d integrated C_l values vs angle of attack compared with pressure tap measurements [4].

In conclusion, Brown et al. [4] demonstrated the feasibility of a non-invasive measurement technique for obtaining wall pressure measurements of a steady state flow, specifically in a Kevlar walled environment. Brown et al.'s [4] method delivers full-field coefficient of pressure distributions along the side wall of a Kevlar test section that was then used to obtain C_l values of a NACA0012 airfoil within 5.4% of traditional pressure taps. According to Brown et al. [4], improvements should be made in the classification of the Kevlar's pre-tensions and material properties to further reduce any uncertainty. The

work of this thesis will take the next step of exploring the possibility of a non-invasive measurement method for transient flows.

2.3 Relevant Fluid Dynamic Concepts

In the field of fluid dynamics, assumptions are frequently made that greatly reduce the complexity of given problems while maintaining accuracy in the results. For example, to correctly model the motion of a viscous fluid, physical laws are used to account for all of the forces that act within the fluid. The conservation of mass and the conservation of momentum are the physical laws used to obtain the equations of motion of the fluid flow [6]. Furthermore, fluids are viscous and the effects of viscous forces and the stresses that act in between neighboring fluid particles must be related to the particle motion [6]. To obtain the equation of motion, a system of coupled nonlinear partial differential equations must be solved [6]. Solving this type of equation can be difficult or time consuming although it is required for most fluid flows. Viscosity is also a crucial parameter for boundary layer theory when a solid body is in a viscous flow. Now, if the boundary layer is thin compared to the solid body, then most of the flow experience no viscous effects [6]. In this case it is common to ignore the effects of viscosity and the viscous stresses in the fluid. A useful fluid dynamic concept that leads to further simplifications is an ideal flow where the flow is assumed to be 2 dimensional, steady, incompressible, irrotational and non-viscous.

An irrotational flow is defined by a flow that contains no vorticity so that $\nabla \times \mathbf{v} = 0$. An initially irrotational flow can only develop vorticity if pressure or viscous forces act on the fluid, for example flow separations and turbulent boundary layers [1]. Vorticity

is calculated by the curl of velocity and this must equal zero in all 3 dimensions for the flow to be considered irrotational. This becomes important as an irrotational vector can be represented as the gradient of a scalar function [6].

The velocity potential is obtained by representing the velocity as the gradient of a scalar function. The velocity potential is a single scalar unknown where the velocity components can be determined [6]. If the flow is incompressible the velocity potential satisfies Laplace's equation:

$$\nabla^2 \phi = \frac{\partial^2 \phi}{\partial x^2} + \frac{\partial^2 \phi}{\partial y^2} + \frac{\partial^2 \phi}{\partial z^2} = 0 \quad (5)$$

For a two-dimensional flow, the solution to Laplace's equation is given by any analytic function of a complex variable. This is conveniently represented by a complex velocity potential:

$$w(z) = \phi + i\psi \quad (6)$$

where ψ is the stream function and will also satisfy Laplace's equation in an irrotational flow and the complex potential is a complex coordinate $z = x_1 + ix_2$. Equation (6) shows that the solution to Laplace equation can be any analytical function of a complex variable [1].

The derivative of the complex potential is then taken to obtain the complex velocity,

$$\frac{dw}{dz} = \frac{\partial \phi}{\partial x_1} + i \frac{\partial \psi}{\partial x_1} = \frac{1}{i} \frac{\partial \phi}{\partial x_2} + \frac{\partial \psi}{\partial x_2} = v_1 - i v_2 \quad (7)$$

Since $v_1 = \frac{\partial \psi}{\partial x_2}$ and $v_2 = -\frac{\partial \psi}{\partial x_1}$ and the complex velocity is simply

$$w'(z) = v_1 - i v_2 \quad (8)$$

Describing the velocity induced by a vortex is obtained by treating the vortex as a singularity in the complex plane and it gives the complex velocity as

$$w'(z) = \frac{i\Gamma}{2\pi(z - z_n)} \quad (9)$$

where Γ is the circulation around the vortex, z is the location of the observer and z_n is the location of the center of the vortex defined as $z_n = x_{1,n} + i x_{2,n}$. The subscript n is used to describe multiple vortices if there are more than one in the flow. For a single vortex located at the origin $x_{1,1} = 0$, $x_{2,1} = 0$ and $z_1 = 0$. This equation is valid for all points other than $z = z_n$ where a singularity occurs resulting in an infinite velocity. Vorticity is restricted to this singularity so that everywhere else the flow is irrotational and any line integral of the velocity over any loop that contains this singularity has a circulation Γ [1].

2.4 Starting Vortex

A starting vortex is created by an airfoil that experiences acceleration or a change in angle of attack. The starting vortex of an airfoil is crucial for the creation of lift [8].

According to Newton, lift is generated by the turning of air and in the case of an airfoil a down wash is produced. The bound vortex, located at the leading edge of the airfoil, is responsible for creating lift and to satisfy the Kelvin's theorem, an equal and opposite vortex must exist somewhere in the flow. This inspired Prandtl to perform experiments in an attempt to pinpoint this other vortex. Prandtl positioned an airfoil inside a wind tunnel with a seeded flow and used cameras to capture the flow at the trailing edge of the airfoil that was accelerated from rest. He was able to successfully photograph a vortex shed spinning in the opposite direction than the bound vortex originating from the trailing edge of the airfoil. This shed vortex mixes with the surrounding downstream air and the motion dies out due to viscous forces [8]. The location of the bound and shed vortex can be seen in figure 6.

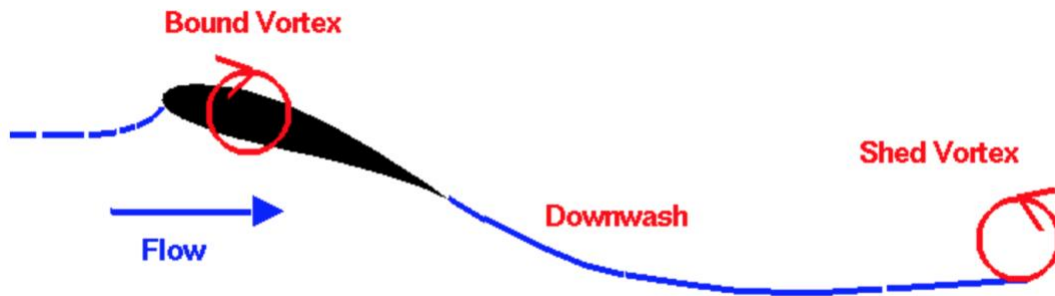


Figure 6: Starting vortex of an Airfoil [8].

To analyze this system, an airfoil can be modeled to be 2D, of infinite span and initially in a stationary flow [1]. To form a closed system, an appropriately sized fluid loop can be outlined around the airfoil that contains all the viscous forces generated by the airfoil during acceleration from rest [1]. Kelvin's Theorem states that the circulation

around this fluid loop will always be zero [1]. During acceleration, a lift force is created as circulation begins to flow around the leading edge of the airfoil [1]. To satisfy Kelvin's Theorem, a circulation that is equal and opposite to the circulation around the leading edge of the airfoil must be present inside the fluid loop, this being the shed vortex [1].

Assuming that the flow is incompressible, the viscous stress on the fluid can be defined as $\mathbf{e} = \frac{\mu}{\rho} \nabla^2 \mathbf{V} = -\nu \nabla \times \boldsymbol{\omega}$. This shows that when the flow is irrotational the viscous force is zero [1]. Consequently, no viscous torques or vorticity can be formed without a boundary [1]. Or in other words viscous forces can only be created at a boundary in the fluid flow such as the one induced by an airfoil [1]. However, as the flow becomes more turbulent the energy becomes more concentrated in turbulent eddies [1]. These eddies can be organized into a vortex street where the vortex train is oscillatory and predictable, or they can become random and unpredictable [1]. It is important to incorporate all these kinds of vortex structures into a model for acoustical analysis because they are a source of sound generation [1], but for simplification, in this study these vortex structures will be omitted, and the flow is assumed to be ideal and completely irrotational.

Chapter 3: The Simple Vortex Model

3.1 Approach

3.1.1 The Simple Vortex Model

This section considers a transient flow based on the startup vortex of an airfoil caused by a step change in angle of attack. The airfoil is represented as a simple vortex located at $\frac{3}{4}$ of the chord length from the trailing edge and its wake is represented as an equal and opposite vortex located at the trailing edge, as shown below in figure 7. The origin is also positioned at the airfoil's trailing edge. The change in angle of attacks is small so the deflection in the x_2 direction is ignored.

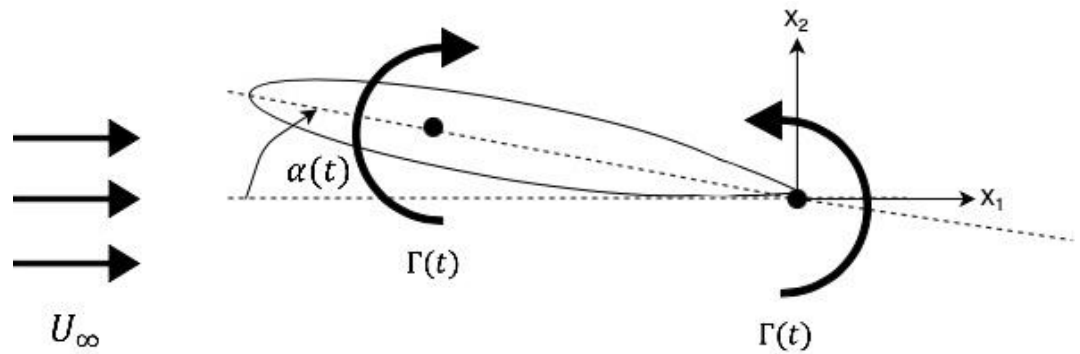


Figure 7: Airfoil Simple Vortex Model.

3.1.2 Vortices, Image Vortices and Wall Boundary Conditions

For simplicity, the vortices in this section are assumed to be two-dimensional and normalized about the vortex strength. Additionally, the flow is assumed to be incompressible, irrotational and non-viscous so that the flow is ideal. Complex potential theory is used to describe the flow and a complex coordinate system is used where the observer location is defined as $z = x_1 + ix_2$ and the distance from the observer to the center of the vortex is defined as $z_n = x_{1,n} + ix_{2,n}$. The subscript n is used to describe multiple vortices if there are more than one in the flow. Now, consider a single vortex in free space positioned at the origin, so that $x_{1,1} = 0$ and $x_{2,1} = 0$ so that $z_1 = 0$ and equation (9) becomes

$$w'(z) = \frac{-i\Gamma}{2\pi(z)} \quad (10)$$

The streamlines of this vortex in free space are shown in figure 8 below. The center of the vortex is located at the origin. The governing equation for this flow is analytical everywhere except at the center of the vortex where a singularity occurs. Here the velocity has a magnitude of infinity. The velocity is a function of radius so as the distance from the center, in this case the origin, increases the velocity decreases.

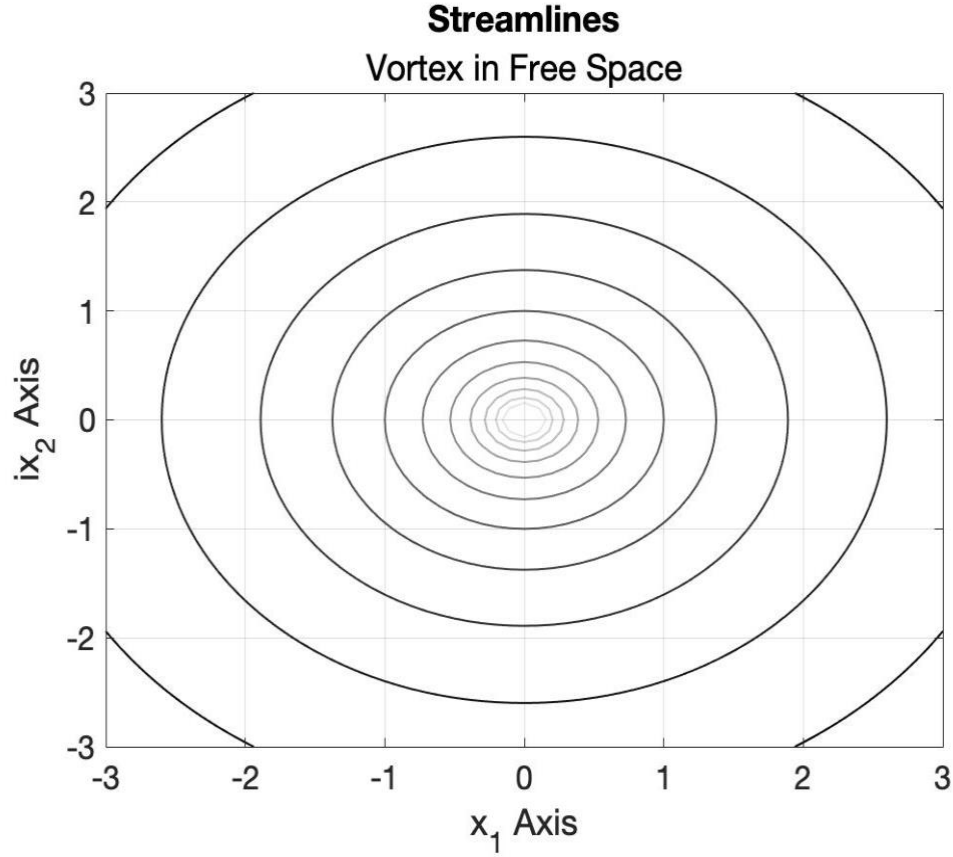


Figure 8: Streamlines of a Vortex in Free Space.

In the case of a vortex positioned near an impervious wall, satisfying the nonpenetration condition along the wall is easily done in complex notation by adding another term to equation (9) [1]. According to the method of images, the effects of solid surface, such as a wall, on a flow are modeled by mirroring the entire flow field about the wall [7]. The wall normal velocities become neutralized, creating a streamline that follows the solid surface and satisfies the nonpenetration condition [1], [7]. For a vortex positioned at the origin a distance h above a wall that is located along the $x_2 = -1$ axis, so that $h=1$, the method of images is used to place an equal and opposite vortex reflected about the $x_2 = -1$ axis. This creates a streamline along the $x_2 = -1$ axis so that there is

no flow normal to this plane [9] The center of this image vortex is located at $x_{1,2} = 0$ and $x_{2,2} = -2ih$ so that $z_2 = -2ih$ and the complex velocity becomes

$$w'(z) = \frac{i\Gamma}{2\pi(z - z_1)} + \frac{-i\Gamma}{2\pi(z - z_2)} = \frac{i\Gamma}{2\pi(z)} + \frac{-i\Gamma}{2\pi(z - 2ih)} \quad (11)$$

These vortices are equal and opposite, so the center of the image vortex is another singularity and the velocity at this point has a magnitude of negative infinity. The streamlines for this flow are shown below in figure 9.

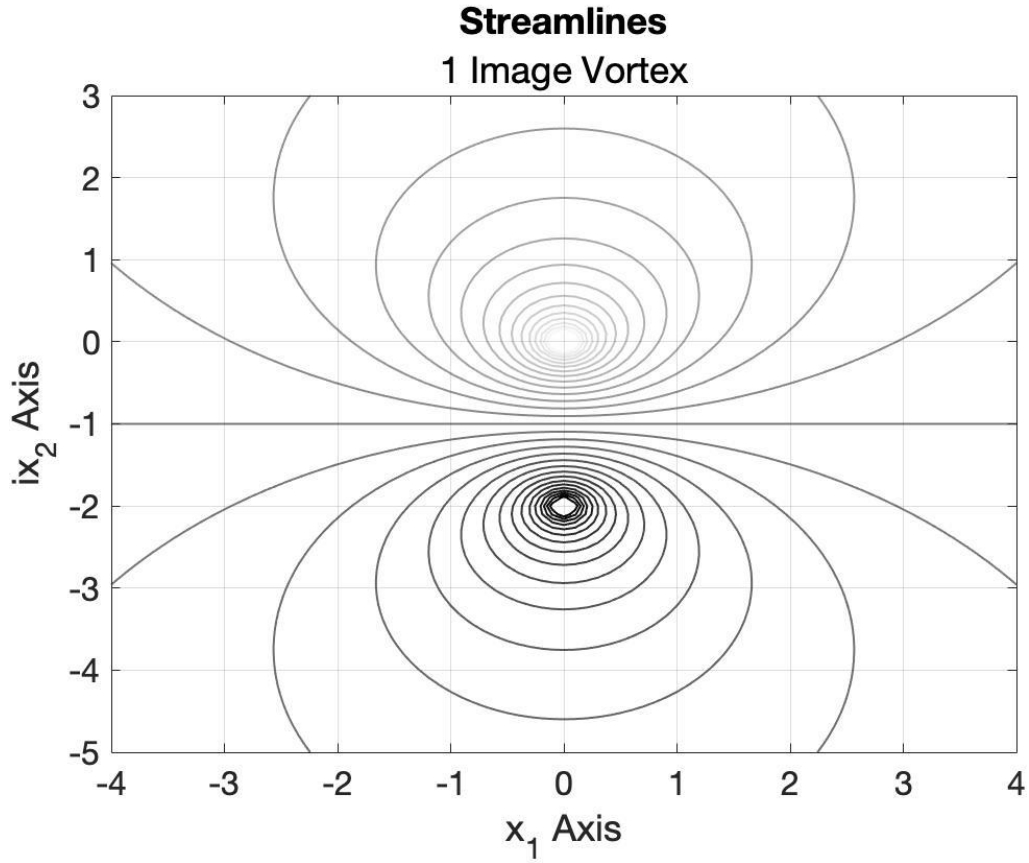


Figure 9: Streamlines of a Vortex with One Image Vortex.

Figure 10 shows the vertical velocity component v_2 along the non-penetration boundary condition that is located normal to the $x_2 = -1$ axis. The vertical velocity component has a magnitude of zero for all locations along the $x_2 = -1$ axis. Therefore, the image vortex satisfies the non-penetration condition along the wall.

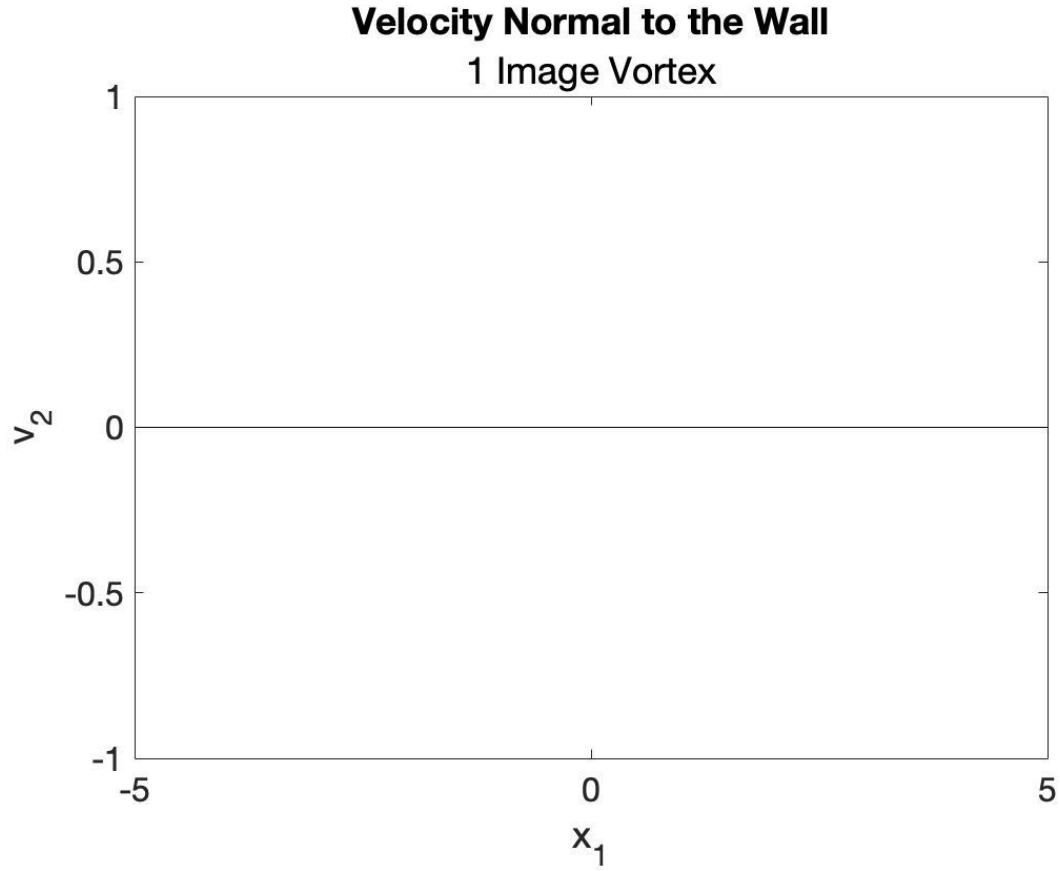


Figure 10: Vertical Component of Velocity Along the Non-Penetration Boundary.

To account for the non-penetration boundary conditions at a second wall, a second image vortex is used. If the second wall is located along the $x_2 = 1$ axis then the second image vortex is reflected about this axis and its center is located at $x_{1,3} = 0$ and $x_{2,3} = 2ih$ so that $z_3 = 2ih$. The complex velocity of this flow becomes

$$w'(z) = \frac{i\Gamma}{2\pi(z)} + \frac{-i\Gamma}{2\pi(z - 2ih)} + \frac{-i\Gamma}{2\pi(z + 2ih)} \quad (12)$$

Both image vortices are equal and opposite to the original vortex. The streamlines for this flow field are shown beneath in figure 11 where the walls are located along the $x_2 = -1$ and $x_2 = 1$ axes.

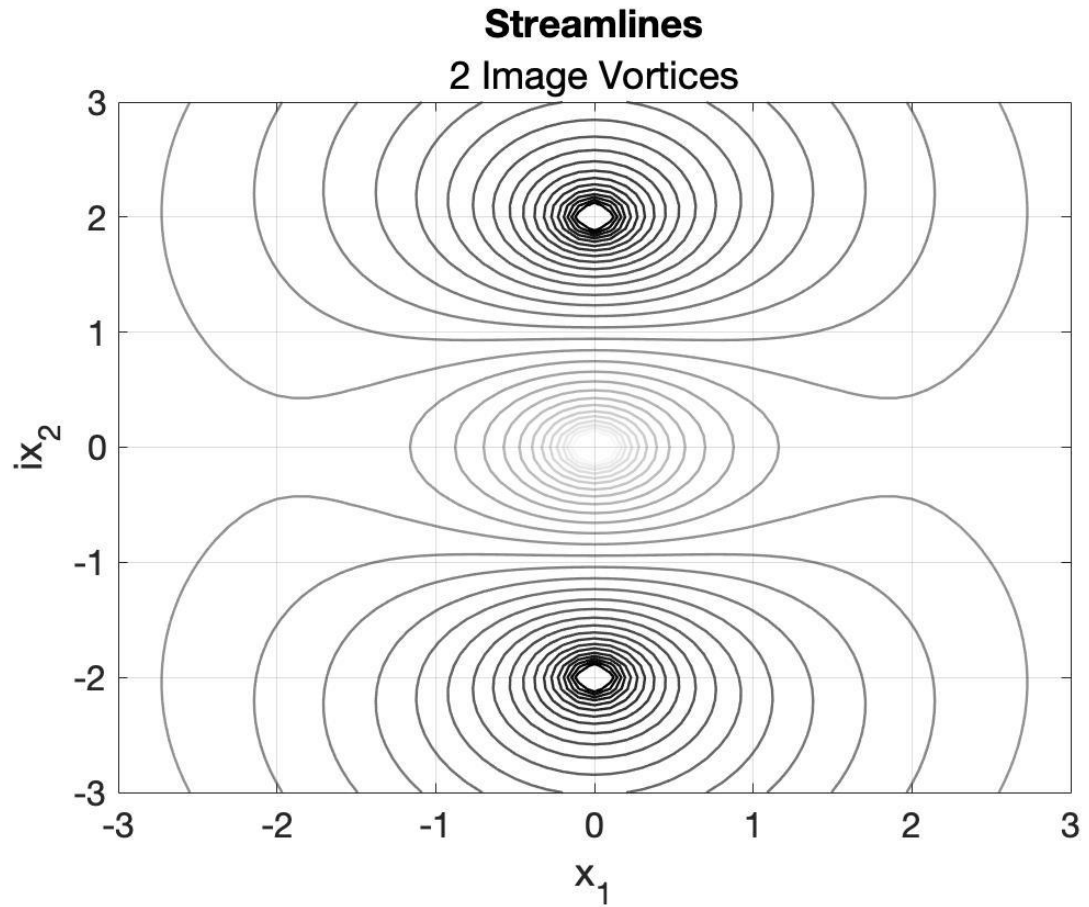


Figure 11: Two Image Vortices.

The velocity component v_2 that is normal to the $x_2 = -1$ plane for this flow is shown below in figure 12. The magnitude is no longer zero, so the non-penetration boundary condition is no longer satisfied. This is a result of the influence that each mirror vortex has on one another.

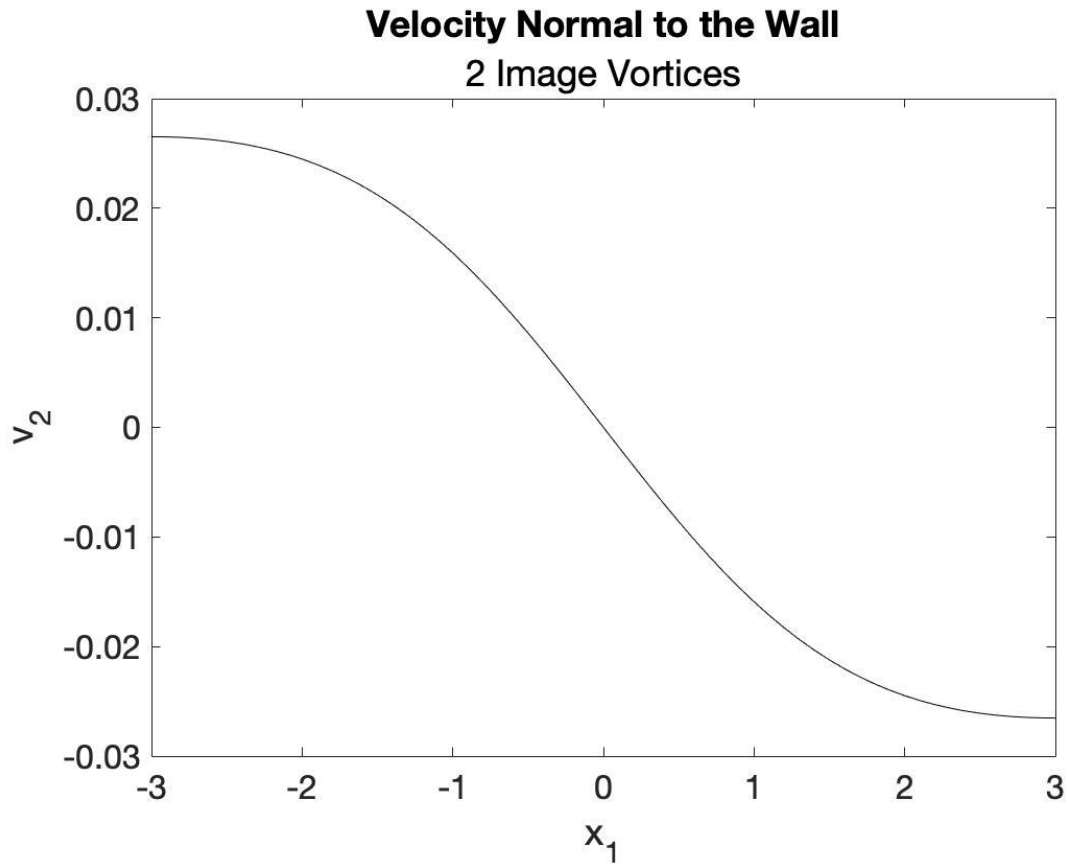


Figure 12: Vertical Component of Velocity Along the Non-Penetration Boundary.

To reduce the influence that these image vortices have on one another, even more image vortices are used. Each additional image vortex will reduce the influence that one has on another at the wall boundary. An infinite amount of image vortices must be used to perfectly recreate the non-penetration boundary condition located along the walls. It is

impossible to compute the flow field for an infinite number of vortices, so a finite number of image vortices is used. The variable N is used to specify how many image vortices are used and n is varied from $-N$ to N in increments of 1 so if $N=10$ then 20 image vortices are used. Since n is varied from $-N$ to N it can equal zero so that original vortex is accounted for when $n=0$. The function $(-1)^n$ is added to oscillate the sign of gamma between negative and positive because each additional set of image vortices have equal but opposite magnitudes.

$$w'(z) = \sum_{n=-N}^N \frac{i\Gamma_n(-1)^n}{2\pi(z - z_n)} \quad (13)$$

The value of N must be appropriately chosen to make the vertical velocity component along the wall sufficiently small, ensuring that the non-penetration boundary conditions are satisfied. The streamlines for this flow are shown below in figure 13. In this case 98 image vortices were used, 49 above and 49 below the trailing edge vortex. The streamline along the $x_2 = -1$ and 1 axes have straightened out. The outer most streamline crosses the path of the free stream velocity inside the wind tunnel, but its magnitude is small compared to the free stream velocity so its influence will be negligible.

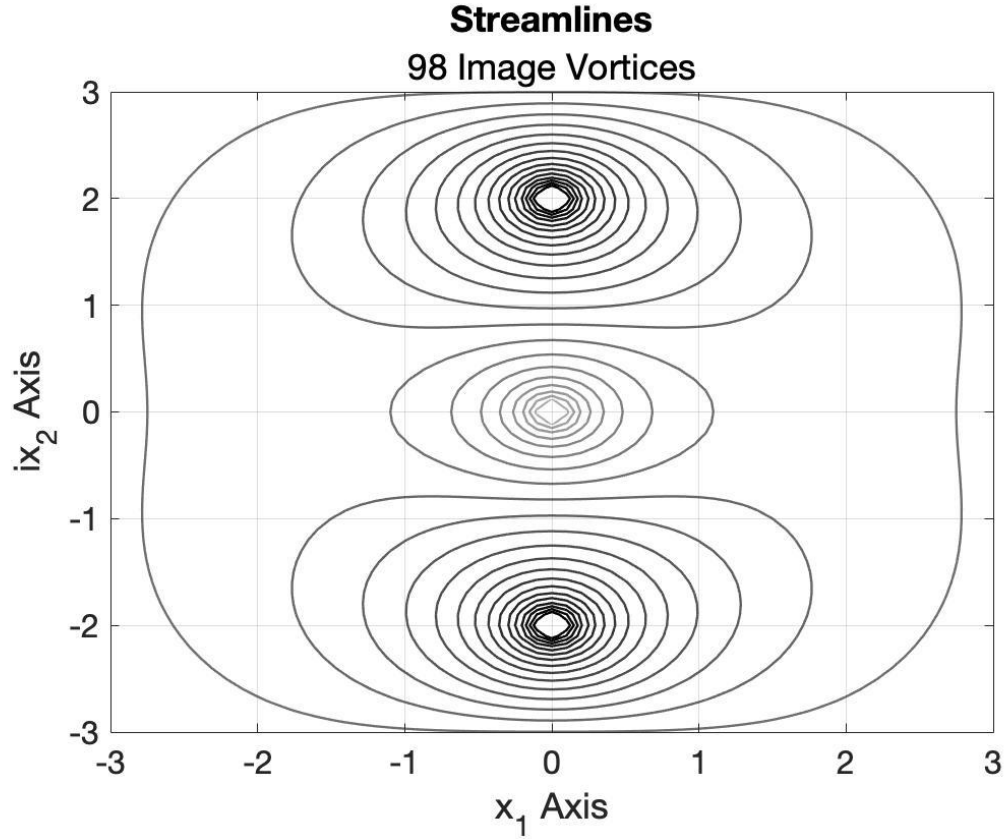


Figure 13: Summation of Image Vortices.

The vertical velocity component v_2 along both walls is shown in figure 14. The magnitude of the vertical velocity component along both walls is now $\sim 10^{-4}$ compared to 10^{-2} in figure 12 when only two image vortices were used. The error has become smaller and will converge to zero as n goes to infinity.

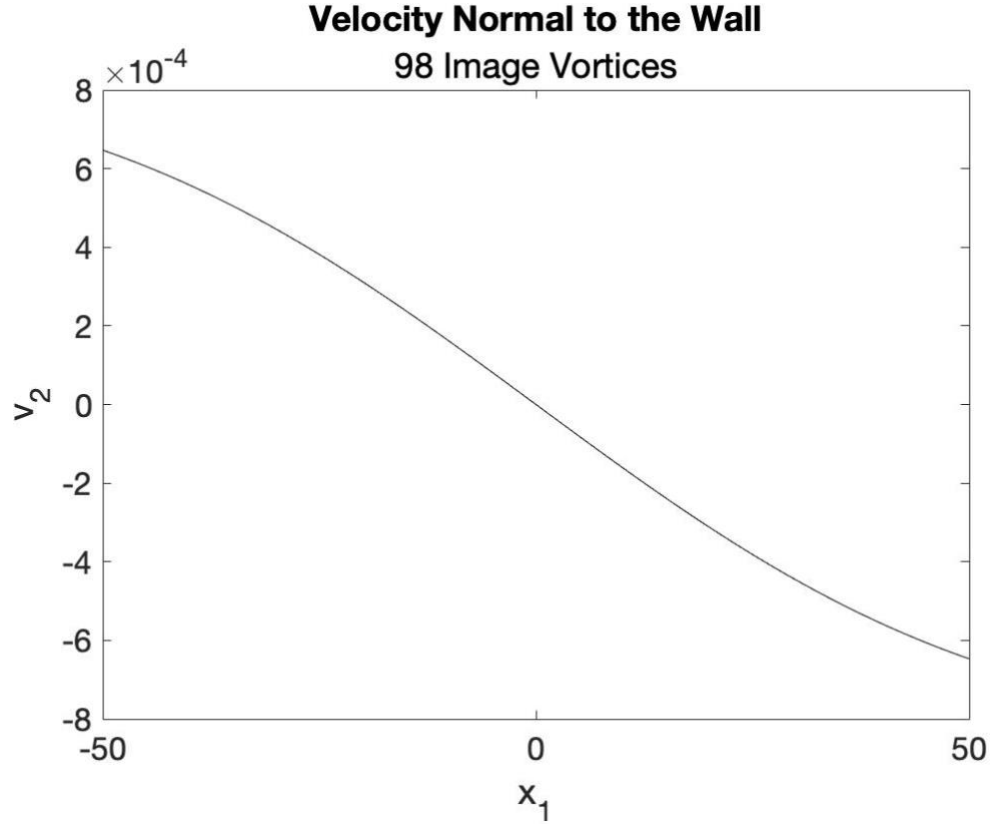


Figure 14: Vertical Velocity Component Along the Non-Penetration Boundary 1 and 2.

In the case of a uniform flow of velocity U_∞ flowing between the 2 walls previously defined, the uniform flow is simply multiplied by z and added to the complex potential so that the complex potential of the entire flow becomes

$$w(z) = U_\infty z - \sum_{n=1}^{\infty} \frac{i\Gamma_n(-1)^n}{2\pi} \ln(z - z_n) \quad (14)$$

and differentiating with respect to z yields the complex velocity

$$w'(z) = U_\infty - \sum_{n=1}^{\infty} \frac{i\Gamma_n(-1)^n}{2\pi(z - z_n)} \quad (15)$$

The pressure at any point is determined by the Bernoulli's equation for unsteady potential flows that gives the relationship between velocity and pressure as

$$\frac{\partial \phi}{\partial t} + \frac{1}{2}v_i^2 + \frac{P}{\rho} = \text{constant} \quad (16)$$

where $\frac{\partial \phi}{\partial t} = \text{Re}\left(\frac{\partial w}{\partial t}\right)$ and $v_i^2 = |w'|^2$. Finally, substituting the complex velocity, setting the constant to zero and solving for $\frac{P}{\rho}$ yields:

$$\begin{aligned} \frac{P}{\rho} = & \text{Re} \left(\sum_{n=-N}^N \frac{i}{2\pi} \left(\frac{d\Gamma_n(-1)^n}{dt} \ln(z - z_n) - \frac{\Gamma_n(-1)^n}{(z - z_n)} \frac{dz_n}{dt} \right) \right) - \frac{1}{2} U_\infty^2 \\ & + \text{Re} \left[\sum_{n=-N}^N \frac{i\Gamma_n(-1)^n U_\infty}{2\pi(z - z_n)} \right] - \frac{1}{2} \left| \sum_{n=-N}^N \frac{\Gamma_n(-1)^n}{2\pi(z - z_n)} \right|^2 \end{aligned} \quad (17)$$

3.1.3 Lift Force, Wagner's Function, and Circulation

The lift force of a 2-dimensional airfoil in an incompressible, unsteady flow of low Mach number is determined by

$$L(t^*) = 4\pi q b \frac{w_o}{U_\infty} \phi(t^*) \quad (18)$$

Here q is the dynamic pressure and is equal to $\frac{\rho_\infty}{2} U_\infty^2$, b is the reference length and is equal to $\frac{c}{2}$, U_∞ is the free stream velocity, w_o is a step gust of constant velocity and $\varphi(t^*)$ is determined by the Wagner's function

$$\varphi(t^*) \cong \frac{t^* + 2}{t^* + 4} \quad (19)$$

where the non dimensional time t^* is defined by $t^* = \frac{U_\infty t}{b}$.

The response of the Wagner function is shown in figure 15. The critical time t_c^* also determined from the Wagner function. In this situation, the critical time is determined by the time that it takes for the Wagner function to converge to 1. This occurs only when $t^* = \infty$ so the critical time must be approximated. The time at which $\varphi(t^*)$ reaches 92% of its true value is used for this approximation. The critical time was found to be $t_c^* = 10$ when $\varphi(t^*) \approx 0.92$ shown in figure 15 with a red star.

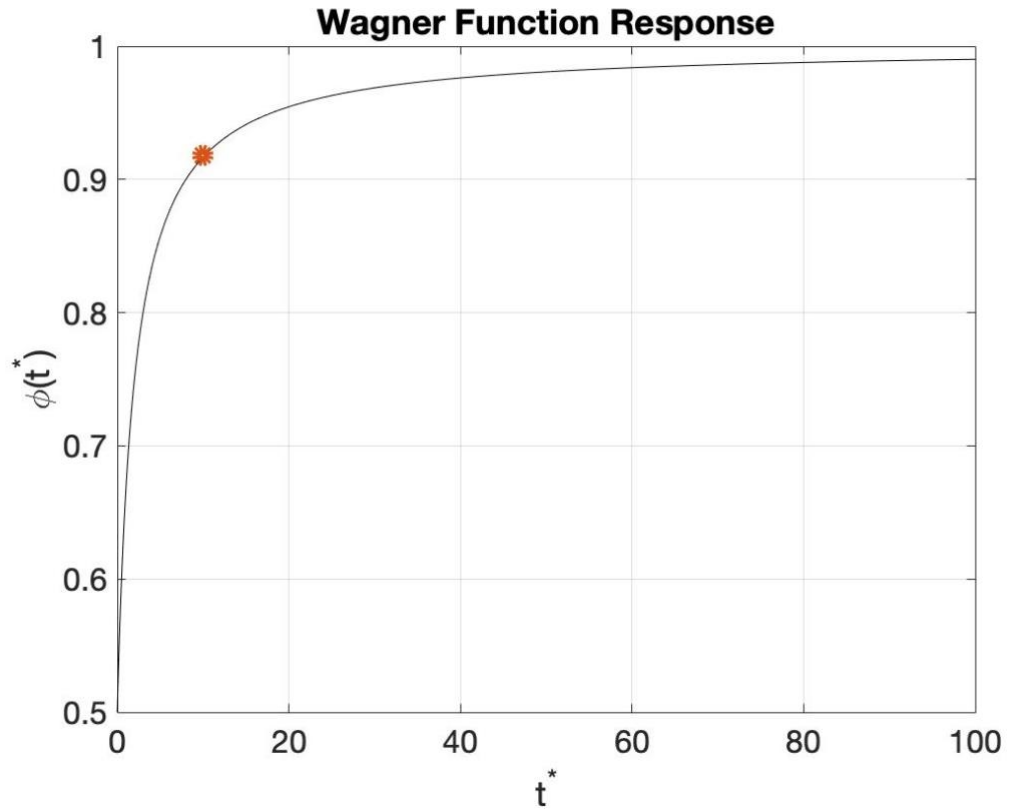


Figure 15: Wagner Function Response.

The coefficient of lift is determined by

$$C_l = \frac{L}{2qb} \quad (20)$$

The circulation around the airfoil is defined as

$$\Gamma_0 = 4bC_lU_\infty \quad (21)$$

3.1.4 Time Less Than the Critical Time

As soon as an airfoil has a change in angle of attack, a bound vortex and a shed vortex begins to form and grow as a function of time. According to Kelvin's theorem, a material contour that contains all the fluid particles in a closed loop must always be zero. Therefore, the bound and the shed vortex must be equal and opposite in strength so that they cancel out and make the total circulation zero. In this case, the bound vortex is fixed at $\frac{3}{4}$ of the chord length from the trailing edge of the airfoil and the shed vortex remains attached at the trailing edge located at the origin, as seen in figure 16.

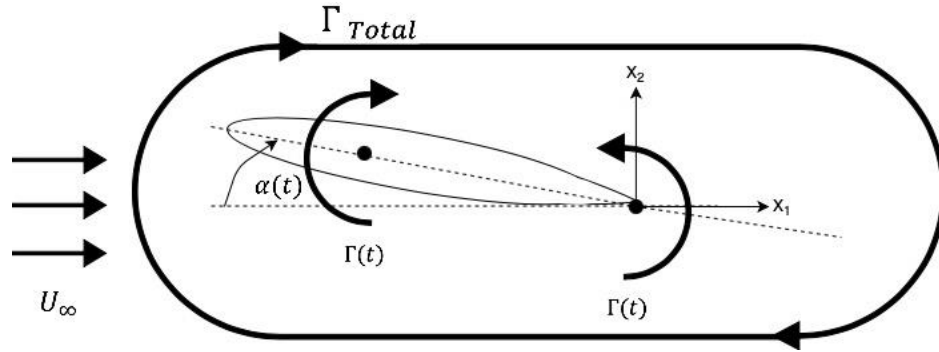


Figure 16: Simple Vortex Model Material Contour.

These vortices continue to grow until a critical time t_c^* . The strength of these vortices for time less than the critical time is determined by

$$\Gamma_n = \Gamma_0 \left(\frac{t^* + 2}{t^* + 4} \right) (-1)^n \quad (22)$$

An expression for the rate of change of vortex strength is found by taking the first derivative with respect to time and is

$$\frac{d\Gamma}{dt^*} = \Gamma_0 \left(\frac{2}{(t^* + 4)^2} \right) (-1)^n \quad (23)$$

The distance from the origin to the observed location x_m is defined as

$$z = x_m - i \frac{h}{2} \quad (24)$$

The bound vortex is positioned $\frac{3}{4}$ of the chord length upstream from the shed vortex and its location is

$$z_c = -0.75c + 2inh \quad (25)$$

The location of the shed vortex is

$$z_n = 2inh \quad (26)$$

The complex potential for this flow field is

$$w(z) = \sum_{n=1}^{\infty} U_{\infty} z + \frac{\Gamma_n}{2\pi} \log(z - z_n) - \frac{\Gamma_n}{2\pi} \log(z - z_c) \quad (27)$$

In this case, there is no convection velocity so $\frac{\partial \phi}{\partial t}$ becomes

$$\frac{\partial \phi}{\partial t} = \text{Re} \left(\frac{dw}{dt} \right) = -\text{Re} \left(\sum_{n=1}^{\infty} \frac{i}{2\pi} \left(\frac{d\Gamma_n}{dt} \ln(z - z_n) - \frac{d\Gamma_n}{dt} \ln(z - z_c) \right) \right) \quad (28)$$

and v_i^2 becomes:

$$v_i^2 = |w'(z)|^2 = U_0^2 + 2\text{Re} \left(- \sum_{n=1}^{\infty} \frac{i\Gamma_n U_{\infty}}{2\pi(z - z_n)} \right) + \left| \sum_{n=1}^{\infty} \frac{\Gamma_n}{2\pi(z - z_n)} \right|^2 \quad (29)$$

Note that the function $(-1)^n$ was accounted for in equation (22) and equation (23).

3.1.5 Time Greater Than the Critical Time

When the critical time is reached, the magnitude of the shed vortex Γ_n converges to a maximum value and its center begins to move down stream at the convection velocity U_c , as seen in figure 17 below. Due to the small angle of attack, the displacement of the bound vortex in the x_2 direction is ignored.

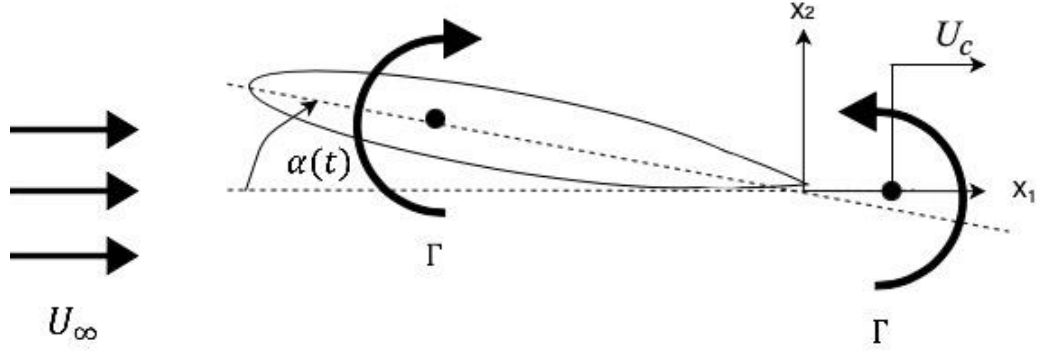


Figure 17: Airfoil Simple Vortex Model Time Greater Than Critical Time.

Since the magnitude of the vortex remains constant, so that $\frac{d\Gamma_n}{dt} = 0$, the circulation is now defined by

$$\Gamma_n = \Gamma_0(-1)^n \quad (30)$$

Since there is no acceleration, the steady state convection velocity U_c is achieved instantaneously and is equal to the free stream velocity so $U_c = U_\infty$. In this case, z and z_c are still determined by equation (24) and (25) respectfully, while the position of the shed vortex x_n is now

$$x_n = c + \int_{t_0}^t U_c dt \quad (31)$$

The position of the center of the shed vortex z_n is now a function of time and is

$$z_n = x_n + 2inh \quad (32)$$

and $\frac{\partial \phi}{\partial t}$ becomes

$$\frac{\partial \phi}{\partial t} = Re \left(\frac{dw}{dt} \right) = -Re \left(\sum_{n=1}^{\infty} \frac{i}{2\pi} \left(\frac{d\Gamma_n}{dt} \ln(z - z_n) - \frac{\Gamma_n U_{\infty}}{(z - z_n)} - \frac{d\Gamma_n}{dt} \ln(z - z_c) \right) \right) \quad (33)$$

and v_i^2 is calculated using equation (29).

3.1.6 Convection Acceleration

If the acceleration of the shed vortex is considered as it begins to convect downstream, then when it separates from the trailing edge, both its strength and position could be a function of time. Furthermore, the convection speed grows as a function of time until the steady state convection velocity U_c is reached. Assuming that the convection speed grows linearly with time and the acceleration time is half of a period, its magnitude can be determined as

$$u(t) = \begin{cases} 0 & \tau < 0 \\ \frac{2U_c \tau}{T} & 0 < \tau < T/2 \\ U_c & \tau > T/2 \end{cases} \quad (34)$$

Here $u(t)$ is the convection speed as a function of time, U_c is the steady state convection velocity, τ is the time after the critical time nondimensionalized by $\frac{U_{\infty}}{b}$, and T is the time

period that the convection velocity takes to reach its mean value nondimensionalized by $\frac{U_\infty}{b}$.

It is crucial for the period T to be modeled correctly because this parameter has a direct influence on the pressure signal along the wall. To illustrate the effects that the period has on the pressure signal, the signal using 6 different time periods was calculated and is shown in section 3.3.2.. A period of $T=50$ was chosen for the analysis in this paper. The only way of obtaining the true time period that the convection velocity takes to reach its mean value is through wind tunnel experiments.

Since both the vortex strength and position could be a function of time, $\frac{\partial \phi}{\partial t}$ in the pressure equation becomes

$$\frac{\partial \phi}{\partial t} = Re \left(\frac{dw}{dt} \right) = -Re \left(\sum_{n=1}^{\infty} \frac{i}{2\pi} \left(\frac{d\Gamma_n}{dt} \ln(z - z_n) - \frac{\Gamma_n}{(z - z_n)} \frac{dz_n}{dt} - \frac{d\Gamma_n}{dt} \ln(z - z_c) \right) \right) \quad (35)$$

Where $\frac{dz_n}{dt}$ is determined by equation (34) and v_i^2 is determined by equation (29). The unsteady circulation $\frac{d\Gamma_n}{dt}$ is unknown and can only be determined through wind tunnel experimentation. In this study the circulation was assumed to be constant so that it is determined by equation (30) and $\frac{d\Gamma_n}{dt} = 0$.

3.2 Wall Pressure Measurements

3.2.1 Wall Pressure Calculation

Assuming an ideal flow, Bernoulli's equation can be applied to obtain the pressure for an unsteady potential flow. Bernoulli's equation for an unsteady potential flow is given by equation (14). Substituting $\frac{\partial \phi}{\partial t} = Re\left(\frac{\partial w}{\partial t}\right)$ and $v_i^2 = |w'|^2$, setting the constant to zero, and solving for P yields:

$$P = -Re\left(\frac{\partial w}{\partial t}\right)\rho - 0.5|w'|^2\rho \quad (36)$$

3.2.2 Coefficient of Pressure

Since the airfoil under investigation is a scaled model its relative pressure field must be used in analysis. Relative pressures are nondimensionalized so that its value is independent of body size. To find relative pressure, the coefficient of pressure

$$C_p = \frac{-Re\left(\frac{dw}{dt}\right) - 0.5|w'|^2}{0.5U_\infty^2} \quad (37)$$

is used.

3.2.3 Pressure Spectrum and Goody Model

As the flow moves parallel along a wall, in this case the test section of the wind tunnel, a turbulent boundary layer is created. This region contains turbulent eddies and rapid pressure fluctuations. These pressure fluctuations are picked up by the wall

mounted pressure sensor. It is important that the signal induced by the boundary layer is significantly smaller than the signal induced by the airfoil. This is determined by comparing the coefficient of pressure of both signals. First the wall pressure frequency spectrum is determined. Goody formulated an empirical model that describes the wall pressure spectrum under a zero-pressure-gradient turbulent boundary layer [10] as

$$\frac{G_{pp}(\omega) U_e}{(\rho_o u_\tau^2)^2 \delta} = \frac{C_2 \left(\frac{\omega \delta}{U_e}\right)^2}{\left[\left(\frac{\omega \delta}{U_e}\right)^2 + C_1\right]^{3.7} + \left[C_3 R_T^{-\frac{4}{7}} \left(\frac{\omega \delta}{U_e}\right)\right]^7} \quad (38)$$

Goody suggests the following constants [1]:

$$C_1 = 0.5, \quad C_2 = 3.0, \quad C_3 = 1.1$$

Here R_T is the ratio of the outer and inner layer timescales [1] and a value of 300 was chosen. The C_{Prms} value is related to the wall pressure spectrum by

$$C_{Prms} = \int G_{pp}(\omega) d\omega * \frac{\left(\frac{u_\tau}{U_e}\right)^2}{2} \quad (39)$$

To evaluate this numerically $d\omega$ is the non dimensional frequency resolution and a value of 0.1 was used, and $\frac{u_\tau}{U_e}$ is the micro to macro turbulent boundary layer scale ratio and it was taken to be 0.036. The C_{Prms} level of the walls turbulent boundary level was

estimated to be 0.01, which is well below the desired pressure signal that is 2 time larger in magnitude.

3.2.4 Noise Estimates and Removal

The signal obtained from a wall mounted pressure sensor is comprised of the pressure wave induced by the airfoil and the pressure fluctuations induced by the wall turbulent boundary layer. The pressure wave induced by the airfoil is the desired signal and the pressure fluctuations induced by the wall turbulent boundary layer is the unwanted signal. This unwanted signal is considered noise and is determined by

$$Noise = G * C_{prms} \quad (40)$$

where G is an array of pseudorandom values drawn from the standard normal distribution.

The signal is now determined as

$$Signal = C_p + Noise \quad (41)$$

The estimated C_{prms} was found to be of the order of 10^{-2} and is relatively small compared to the C_p values that peak around 1.6. To ensure that the desired pressure signal can be obtained during possible future wind tunnel experiments, a noise levels of 10 times the magnitude of C_{prms} will be used.

3.3 Simple Vortex Model Results

3.3.1 Pressure Time History

The pressure time history for the simple vortex model is determined by computing the coefficient of pressure for a single location along the wall for every time instant.

When this data is plotted, the pressure wave is revealed. Figure 18 shows the pressure time history for a transducer located in the wind tunnel wall at the mid chord point. The signal at this location is positive with a clear peak occurring quickly after the critical time and then the signal converges more slowly to its maximum value. The dashed line is an estimate of the rms pressure on the wind tunnel wall. It was determined that the desired pressure signal was much greater than the background noise produced by the turbulent boundary layer along the wall.

The pressure time history for the simple vortex model is continuous for time before and after the critical time, but at the critical time a discontinuity occurs. This discontinuity is an artifact of using Wagner's function and a discrete vortex model to describe the unsteady circulation and lift of the airfoil. In the following section we will give an alternative analysis that uses Laplace transforms to determine the time history and this changes that nature of the discontinuity in the time history.

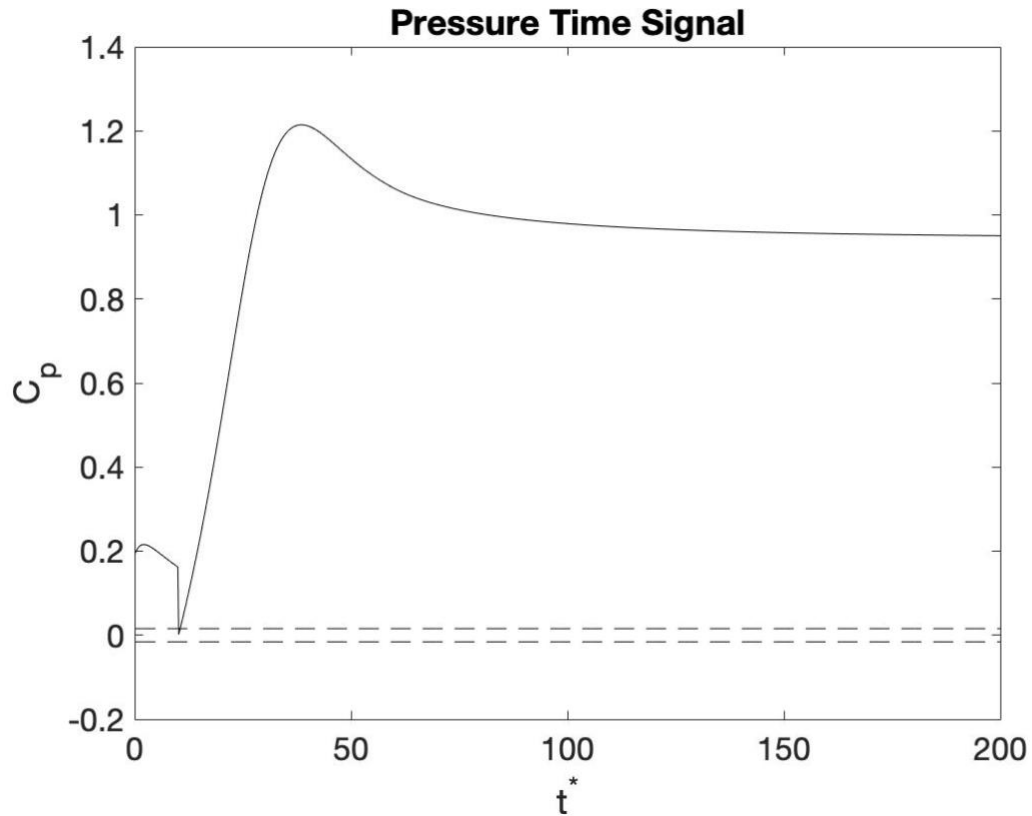


Figure 18: The pressure time history for a transducer located in the wind tunnel wall at the mid chord point.

The pressure time history for a transducer located in the wind tunnel wall at one chord length downstream is shown in figure 19. At this location the signal is transitioning to a negative signal because the signal is a mix of the effects of the airfoil vortex and the wake vortex. This is not an ideal location to place a transducer because the wake signature is very much smaller than the signature of the airfoil vortex and it would be difficult to isolate the two.

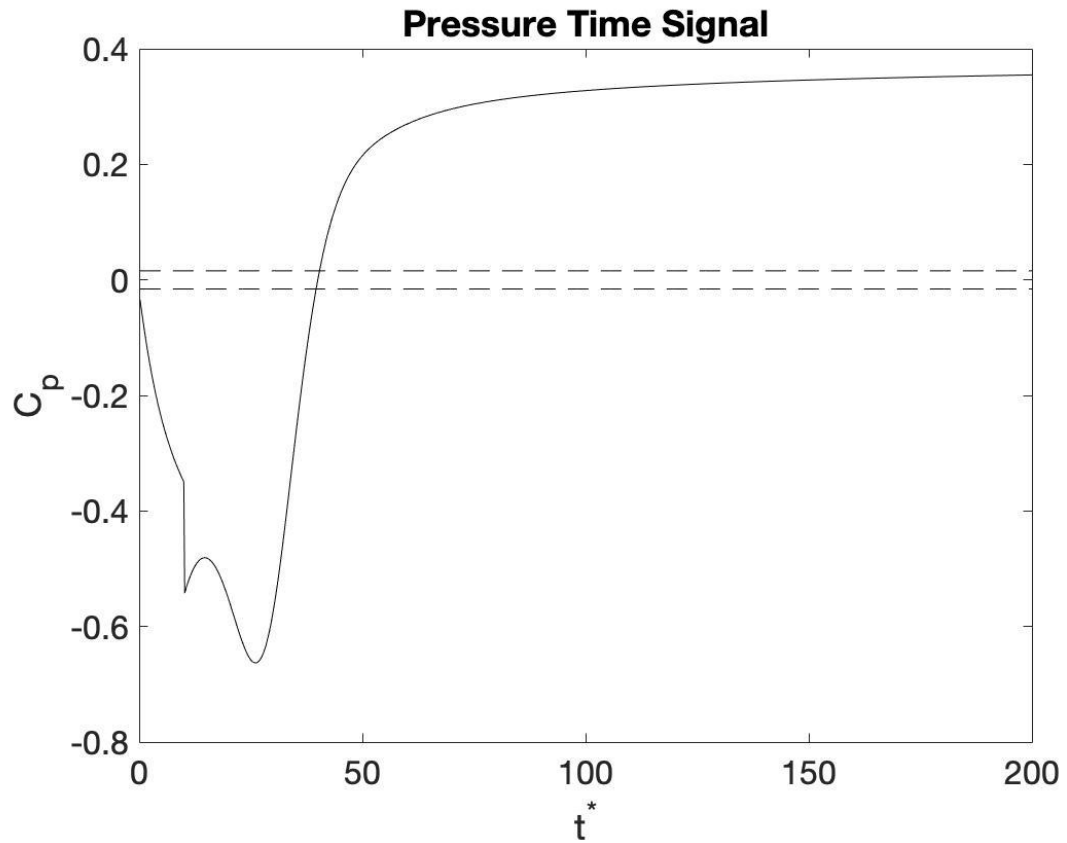


Figure 19: The pressure time history for a transducer located in the wind tunnel wall at 1 chord length downstream.

The pressure time history for a transducer located in the wind tunnel wall at 3 chord lengths downstream is shown in figure 20. This signal is well defined and is completely negative. This is an ideal location for a transducer to be placed because only the signature from the wake vortex is measured.

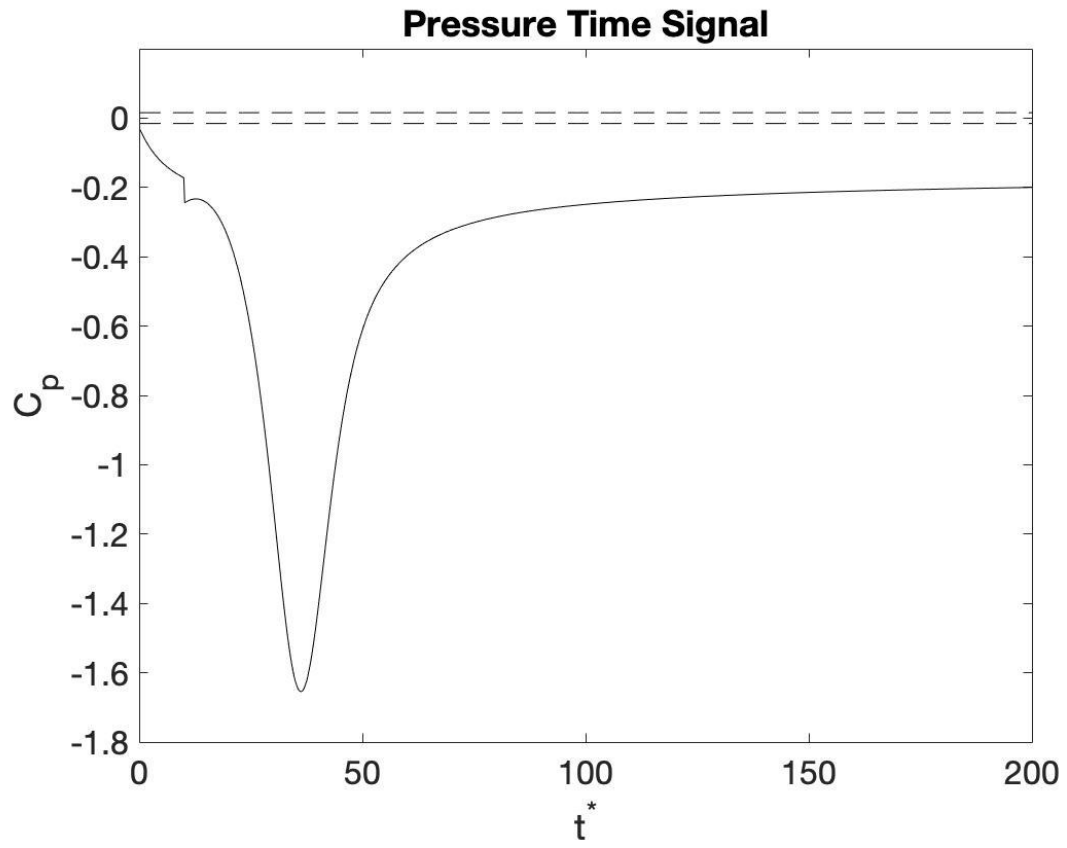


Figure 20: The pressure time history for a transducer located in the wind tunnel wall at 3 chord lengths downstream.

3.3.2 Pressure Time History for Various Convection Acceleration Time Periods

The convection acceleration period plays a crucial role in the shed vortex model. The convection acceleration period is unknown, and its true value can only be obtained through wind tunnel experimentation. In this case the convection speed is assumed to grow linearly with time and that the acceleration time is half of a period. Equation (34) was used to model the convection velocity. Since the convection acceleration period is unknown, 6 different periods were explored for 3 different locations being the mid chord, 1 chord length downstream, and 3 chord lengths downstream.

The results in figure 21 illustrates the effects that the convection acceleration has on the signal obtained at half the chord length. The dashed lines represent the estimated noise levels. At shorter periods, the pressure signal peaks more abruptly and at a larger magnitude. This makes sense intuitively. At longer periods, the pressure signal takes more time to peak, and the peak is smaller in magnitude.

Various Convection Acceleration Periods for Location $x = -0.5$

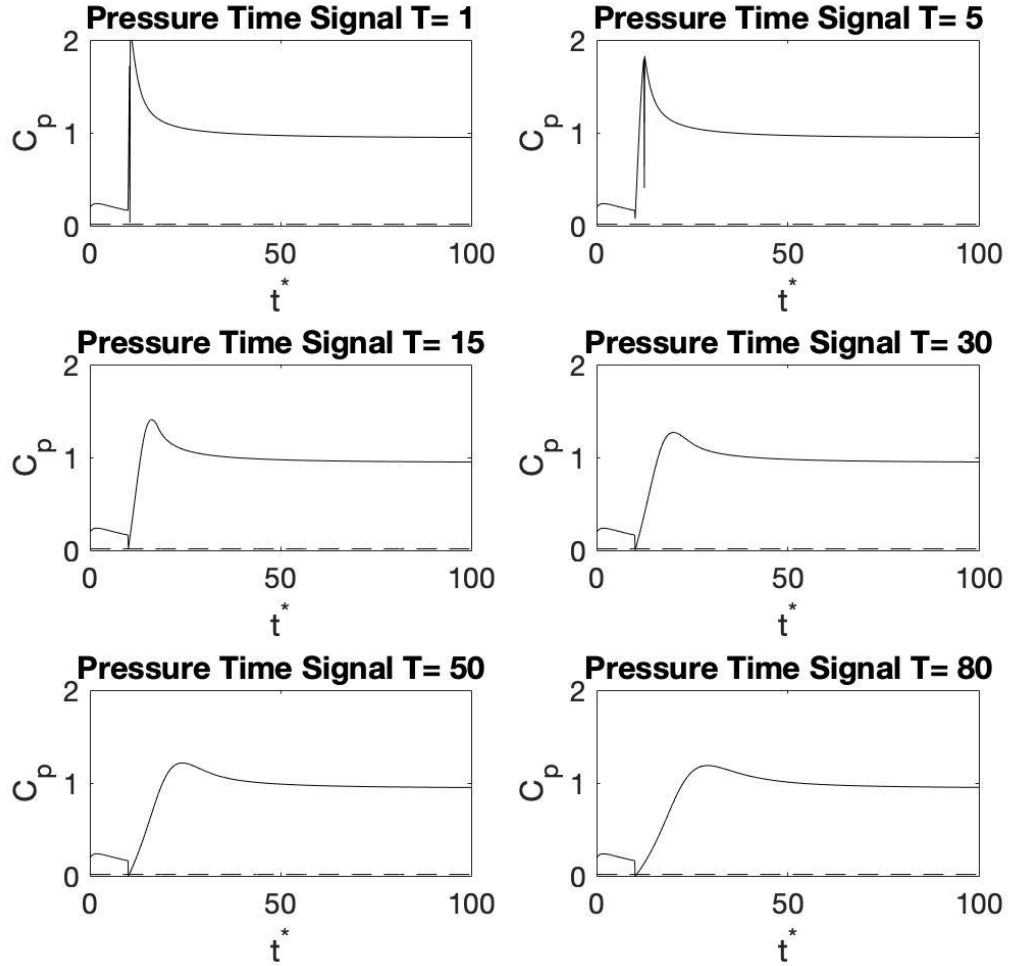


Figure 21: wall pressure signal taken at the mid chord for six different convection acceleration periods

The wall pressure signal obtained at one chord length downstream for six different convection acceleration periods is shown in figure 22. The results are similar to the signal obtained at half the chord length except the signal is in the process of changing from positive to negative. The convection acceleration period has a strong influence on the shape and sign of the pressure signal at this location.

Various Convection Acceleration Periods for Location $x = 1$

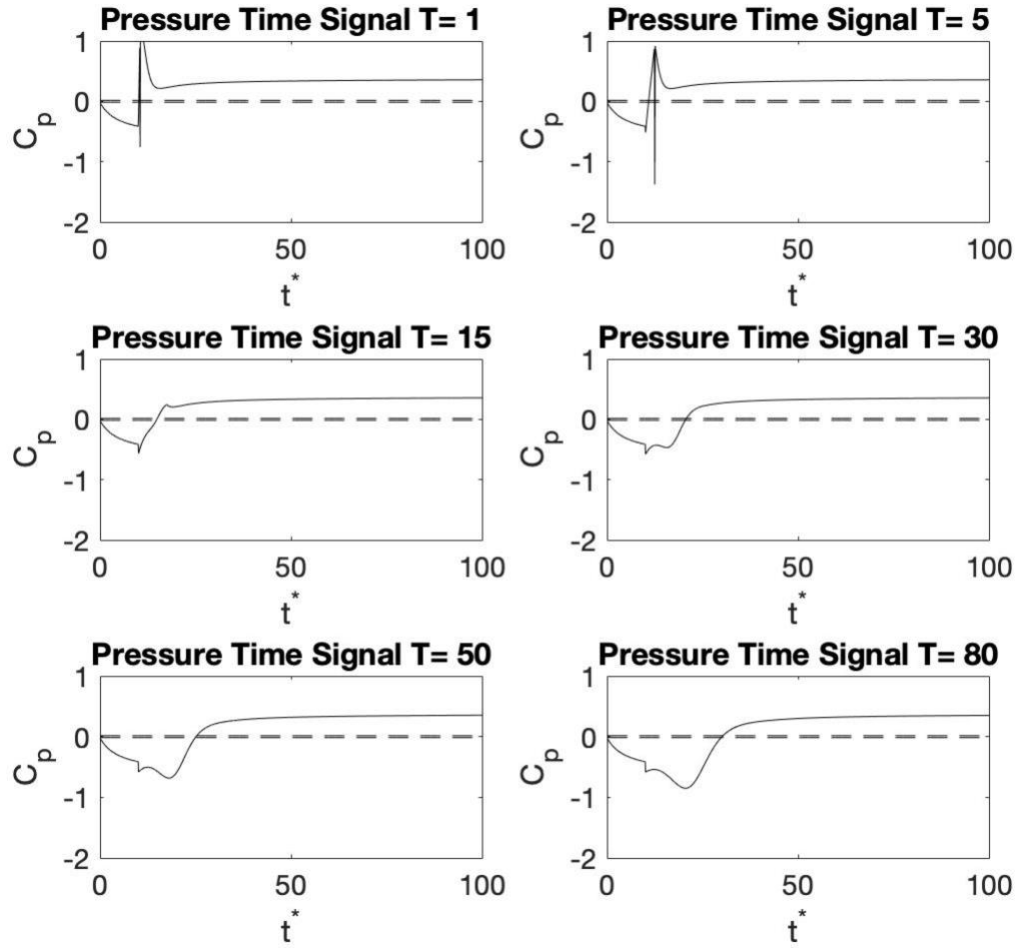


Figure 22: Wall pressure signal taken one chord length downstream for six different convection acceleration periods.

The wall pressure signal taken 3 chord lengths downstream for six different convection acceleration periods is shown in figure 23. At this location, the peak of the pressure wave becomes larger at longer periods. The convection acceleration period also has a strong influence on the shape and sign of the pressure signal at this location.

Various Convection Acceleration Periods for Location $x = 3$

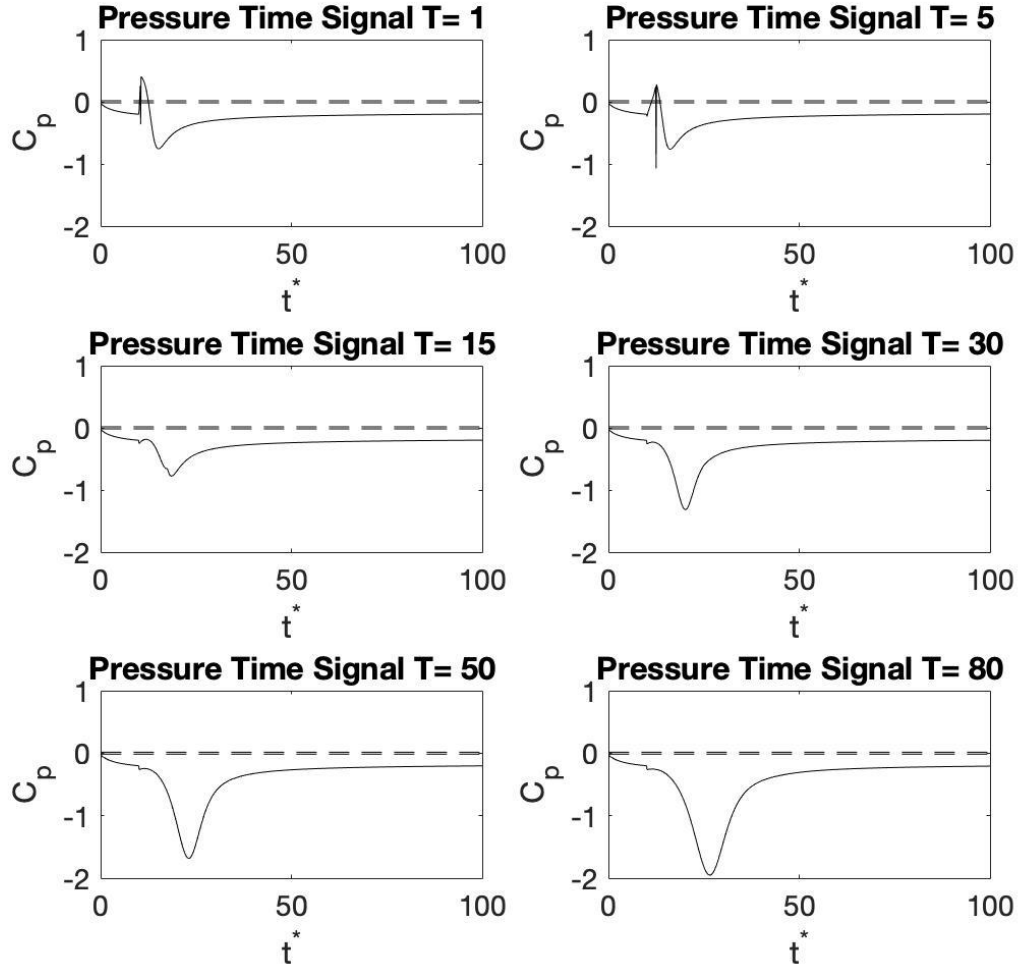


Figure 23: Wall pressure signal taken 3 chord lengths downstream for six different convection acceleration periods.

3.3.3 Spectral Analysis and Filtering

The signal is now a mixture of the desired pressure wave and background noise. The signal with noise for a transducer 3 chord lengths downstream and a convection acceleration period of $T=50$ is shown in figure 21A. The signal is discrete because it is created with a finite time increment. For discrete signals, a digital filter was used to filter out noise. Before the filter can be designed, the signal is transformed from the time

domain to the frequency domain with a Fourier Transform to reveal what frequencies are contained in the signal. The single sided power spectral density is shown in figure 24B. The signal of the desired pressure is determined to have a frequency in the order of 10^{-1} according to the spikes in intensity in the spectral density in the range of 0 to 0.1 where the frequency axis is nondimensionalized by $\frac{b}{U_{\infty}}$. The gaussian noise is shown in the power spectral density as smaller random spikes that are evenly distributed about all frequencies. A digital FIR bandpass filter was used to filter the signal and the cut off frequencies were chosen to be 0 and 0.1 nondimensionalized units based on the spectral analysis. A filter with an order of 20 was used to remove the noise. The filter response is shown in figure 24C, and the filtered signal is shown in figure 24D.

Spectral Analysis of Signal 3 Chord Lengths Downstream and $T=50$

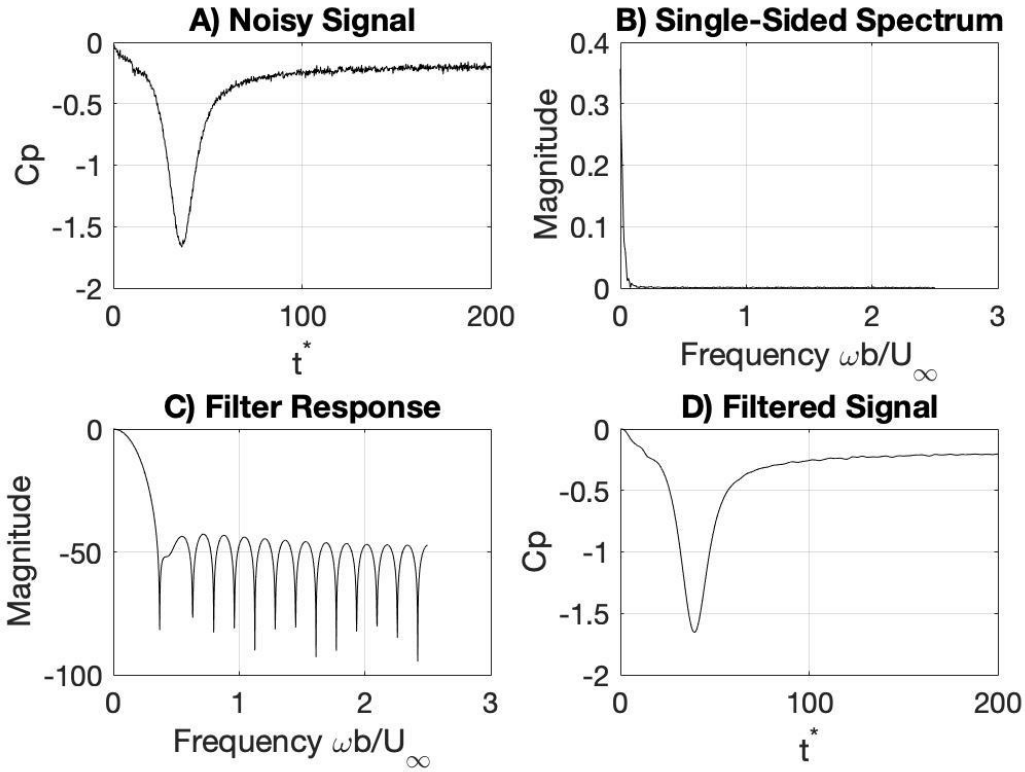


Figure 24: Spectral Analysis of Signal located 3 Chord Lengths Downstream With $T=30$ and the Estimated Amount of Background Noise.

Now a noise level of 10 times the magnitude of C_{prms} was used to ensure that the desired signal can be obtained during possible future wind tunnel experiments. The signal with 10 times the noise is shown in figure 25A. The single sided power spectral density is shown in figure 25B. A digital FIR bandpass filter was used to filter the signal and the cut off frequencies were chosen to be 0 and 0.1 nondimensionalized units. A filter with an order of 30 was used to remove the noise. The filtered signal is shown in figure 25D. The filter was able to remove enough noise for the pressure wave to be obtained at 10 times the estimated noise levels.

Spectral Analysis of Signal 3 Chord Lengths Downstream and $T=50$

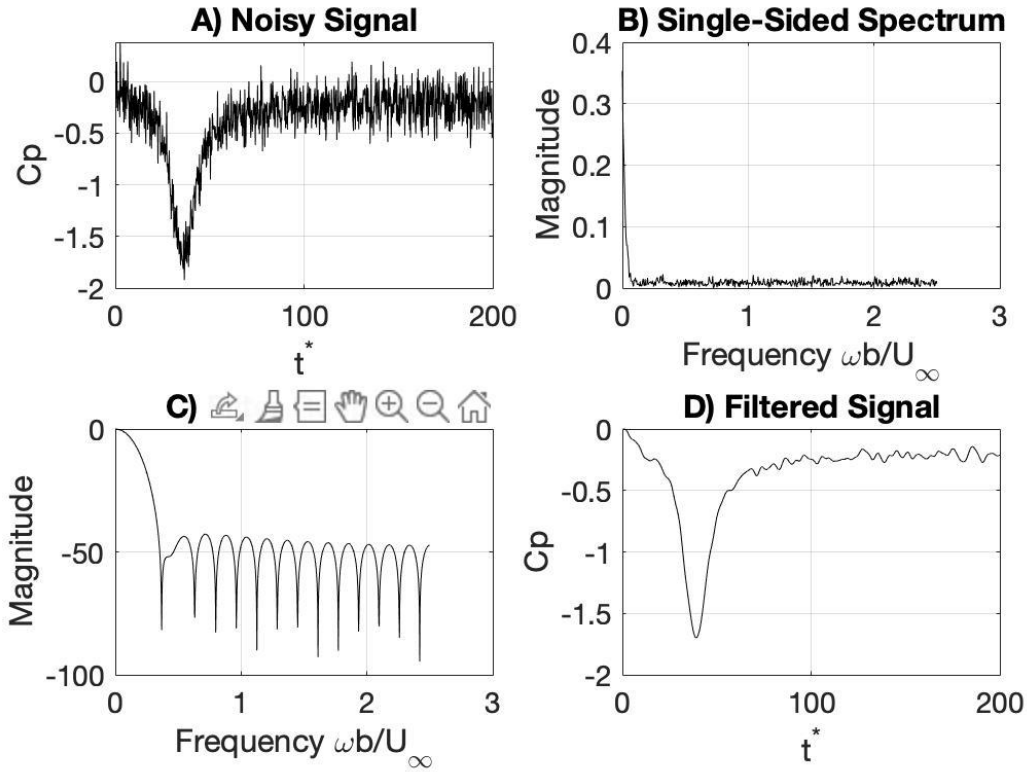


Figure 25: Spectral Analysis of Signal located 3 Chord Lengths Downstream With $T=30$ and 10 Times the Estimated Amount of Background Noise.

3.4 Simple Vortex Model Conclusions

- The critical time at which the starting vortex of an airfoil separates and begins to convect downstream was determined by the Wagner's function at 92 percent of its true value. Furthermore, the unsteady circulation and lift were determined by the Wagner's function which created a discontinuity in the pressure time signal. This is an unrealistic result. The critical time should be investigated more accurately via physical wind tunnel experiments to obtain a more realistic model.
- The acceleration of the starting vortex as it begins to convect downstream was assumed to grow linearly with time and to reach a mean value at half of the

period of acceleration. The convection acceleration period has a direct effect on the pressure signature along the wall and its true value is only determined by physical wind tunnel experiments. Since the acceleration period is unknown, 6 different values were explored and a time period of $T=50$ was chosen for the simple vortex model.

- Goody's model of wall pressure frequency spectrum for a turbulent boundary layer was used to estimate the background noise. The rms estimates were much smaller than the desired pressure wave from the startup vortex of the airfoil. The estimated $C_{p_{rms}}$ was found to be of the order of 10^{-2} and is relatively small compared to the C_p values that peak around 2.2. A digital bandpass filter was about to remove noise from the signal at 10 times the estimated background noise. Therefore, the signal induced by the airfoil is sufficiently large enough to be obtained by a wall mounted pressure transducer.
- The proposed measurement technique can measure features of a transient flow, but physical wind tunnel experiments are required to determine its accuracy.

Chapter 4. Vortex Sheet Model and Kevlar Membrane Response

4.1 Approach

4.1.1 Vortex Sheet Model

This section uses unsteady thin airfoil theory to calculate the wall pressure on a wind tunnel wall due to the transient motion of an airfoil in the test section. Using thin airfoil theory the airfoil and its wake is represented by a vortex sheet of strength $\gamma(x,t)$, as shown below in figure 26. Here all length variables are normalized on the semi-chord of the airfoil $c/2$ and time by $c/2U$ where c is the airfoil chord and U the free stream velocity. The pressure is normalized by ρU^2 , the velocity potential and circulation by $Uc/2$ and the vortex sheet strength by U . The circulation that is shed from the trailing edge is convected downstream in the wake at the speed of the free stream. No period of acceleration is used for the vortex convection speed as was discussed in the previous chapter, so the vortex is assumed to instantaneously convect at the free stream velocity. The origin of the coordinate system is defined to be at the blade trailing edge, so the airfoil is defined along the surface on the x -axis where $-2 < x < 0$ and the wake is on the x -axis where $x > 0$. The displacement of the airfoil in the y direction is ignored and this is valid for thin airfoil theory. The effect of the wind tunnel's walls has been investigated in detail in section 3 but in this section the effects have been omitted.

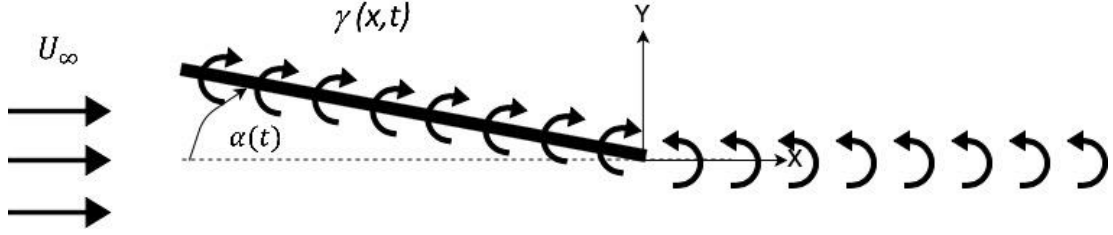


Figure 26: Vortex Sheet Model.

4.1.2 Pressure Calculation

The velocity potential from this vortex sheet is defined from potential flow theory as

$$\phi(z, t) = Ux + \frac{-1}{2\pi} \operatorname{Re} \left(\int_{-2}^0 i\gamma(\zeta, t) \ln(z - \zeta) d\zeta + \int_0^{Ut} i\gamma_w \left(t - \frac{\zeta}{U} \right) \ln(z - \zeta) d\zeta \right) \quad (42)$$

Where $z = x + iy$ is the location in the flow where the potential is defined and $g_w(t)$ is the vortex sheet strength at $z=0$ at time t that is convected downstream at speed U . The net circulation around the airfoil is defined as a function of time as

$$\Gamma(t) = \left(\int_{-2}^0 \gamma(\zeta, t) d\zeta \right) \quad (43)$$

And from Kelvins theorem the net circulation in the flow is constant, so

$$\frac{d\Gamma(t)}{dt} + \frac{d}{dt} \int_0^{Ut} \gamma_w \left(t - \frac{\zeta}{U} \right) d\zeta = 0 \quad (44)$$

However, if the airfoil motion is initiated at time $t=0$ then we find that, by setting $z=Ut$ that

$$\frac{d\Gamma(t)}{dt} = -U \frac{d}{dt} \int_0^t \gamma_w(t - \tau) d\tau = -U\gamma_w(t) \quad (45)$$

The right side of this equation is simply the vortex sheet strength at the trailing edge as a function of time so that the wake circulation is determined from the rate of change of the total circulation about the airfoil.

If the airfoil is replaced by a single vortex located at x_o then we can define the velocity potential as

$$\phi(z, t) = Ux + \frac{-1}{2\pi} \text{Re} \left(i\Gamma(t) \ln(z - x_o) + iU \int_0^t \gamma_w(t - \tau) \ln(z - U\tau) d\tau \right) \quad (46)$$

We can specify the pressure at any point in the flow using Bournoulli's equation for an unsteady flow, which in normalized form is

$$p = -\frac{\partial \phi}{\partial t} - \frac{1}{2} v_i^2 \quad (47)$$

Where

$$v_i^2 = U^2 + U \frac{\partial \phi}{\partial x} + |w'|^2 \quad (48)$$

And

$$w' = -\frac{i\Gamma(t)}{2\pi(z - x_o)} - iU \int_0^t \frac{\gamma_w(t - \tau)}{2\pi(z - U\tau)} d\tau \quad (49)$$

However, this term can be ignored if $U \gg |w'|$. Some care is required when evaluating $\partial f / \partial t$ and by using the identity

$$\frac{\partial}{\partial t} \int_0^t f(\tau, t) d\tau = f(t, t) + \int_0^t \frac{\partial f(\tau, t)}{\partial t} d\tau \quad (50)$$

We find that

$$\begin{aligned} \frac{\partial \phi(z, t)}{\partial t} = \frac{-1}{2\pi} \text{Re} \left(\frac{id\Gamma(t)}{dt} \ln(z - x_o) + iU\gamma_w(0) \ln(z - Ut) \right. \\ \left. + iU \int_0^t \frac{\partial \gamma_w(t - \tau)}{\partial t} \ln(z - U\tau) d\tau \right) \end{aligned} \quad (51)$$

Evaluating the last integral by parts, and noting that $\partial g_w(t-t)/\partial t = -\partial g_w(t-t)/\partial t$ gives

$$\begin{aligned} \frac{\partial \phi(z, t)}{\partial t} = & \frac{-1}{2\pi} \text{Re} \left(\frac{id\Gamma(t)}{dt} \ln(z - x_o) + iU\gamma_w(0) \ln(z - Ut) - iU\gamma_w(0) \ln(z - Ut) \right. \\ & \left. + iU\gamma_w(t) \ln(z) - iU \int_0^t \frac{\gamma_w(t - \tau)}{z - U\tau} d\tau \right) \end{aligned} \quad (52)$$

Next consider $U\partial f/\partial x$ which is

$$U \frac{\partial \phi(z, t)}{\partial x} = \frac{-U}{2\pi} \text{Re} \left(\frac{i\Gamma(t)}{(z - x_o)} + iU \int_0^t \frac{\gamma_w(t - \tau)}{z - U\tau} d\tau \right) \quad (53)$$

Then adding these two terms gives

$$\frac{\partial \phi(z, t)}{\partial t} + U \frac{\partial \phi(z, t)}{\partial x} = \frac{-1}{2\pi} \text{Re} \left(\frac{id\Gamma(t)}{dt} \ln(z - x_o) + iU\gamma_w(t) \ln(z) - \frac{iU\Gamma(t)}{(z - x_o)} \right) \quad (54)$$

And replacing g_w gives

$$\frac{\partial \phi(z, t)}{\partial t} + U \frac{\partial \phi(z, t)}{\partial x} = \frac{-1}{2\pi} \text{Re} \left(\frac{id\Gamma(t)}{dt} \ln \left(1 - \frac{x_o}{z} \right) - \frac{iU\Gamma(t)}{(z - x_o)} \right) \quad (55)$$

It follows that the contribution from the wake is only determined by the nonlinear term $v_i'^2$

which decays as $1/|z|^2$ so it will be much smaller in magnitude. Also note that for $|z| \gg x_o$

it can use the approximation $\ln(1-x_o/z)=x_o/z+....$ to show that the pressure decays as $1/z$ at large distances for both terms in the above equation. The pressure perturbation is then

$$p(t) = \frac{-1}{2\pi} \text{Re} \left(\frac{id\Gamma(t)}{dt} \ln \left(1 - \frac{x_o}{z} \right) - \frac{iU\Gamma(t)}{(z - x_o)} \right) - \frac{1}{2} |w'|^2 \quad (56)$$

The Wagner function gives the variation of lift after a step change in angle of attack as a jump that is half the magnitude of the final lift followed by a slow increase that depends on $(t+2)/(t+4)L_{max}$ or

$$L_{max}(1 - ae^{-\alpha t} - be^{-\beta t}) \quad (57)$$

With $a=0.165, b=0.335, \alpha=0.0455, \beta=0.3$.

Since the circulation and the lift are related by $L=rGU$ and the results can be written in terms of the maximum, or final, circulation so we obtain

$$p(t) = \frac{\Gamma_{max}}{2\pi} \text{Im} \left(\frac{f^{(1)}(t)}{(z - x_o)} - f^{(2)}(t) \ln \left(1 - \frac{x_o}{z} \right) \right) - \frac{1}{2} |w'|^2 \quad (58)$$

Where $f^{(2)}(t)=\partial f^{(1)}/\partial t$.

$$f^{(1)}(t) = 1 - ae^{-\alpha t} - be^{-\beta t} \quad (59)$$

$$f^{(2)}(t) = \frac{\delta(t)}{2} + H(t)(a\alpha e^{-\alpha t} + b\beta e^{-\beta t}) \quad (60)$$

To obtain the pressure at a point this result is multiplied by rU^2 .

4.1.3 Membrane Response

The equation of motion for the displacement of a tensioned membrane is given by the wave equation

$$\frac{\partial^2 \zeta}{\partial x'^2} + \frac{\partial^2 \zeta}{\partial y'^2} - \frac{1}{c_t^2} \frac{\partial^2 \zeta}{\partial t^2} = -\frac{p(x', y', t)}{m_a c_t^2} \quad (61)$$

Where z is the surface displacement, the membrane coordinates are x', y' where y' is along the span and x' is in the direction of the flow. If the trailing edge of the airfoil is at $x' = x_c'$ then $x = x' - x_c'$. Also, $c_t = (\partial T / r_a)^{1/2} / U$ is the speed of the wave in the membrane non-dimensionalized by the free stream speed, and $r_a = 58 \text{ gm/m}^2$ is the mass per unit area, and the tension per unit length is $\partial T = 50 \text{ N/m}$ so $c_t = 29.36 / U$. To be consistent with the normalization used above, the pressure p is non dimensional, all lengths are normalized on $c/2$, time by $c/2U$ and $m_a = 2r_a / r_o c$.

To solve this equation, the displacement is expanded in the membrane modes that satisfy the boundary conditions at the edges of the membrane

$$\zeta(x', y', t) = \sum_{m=1}^{\infty} \sum_{n=1}^{\infty} A_{mn}(t) \Phi_{mn}(x', y') \quad (62)$$

Where

$$\Phi_{mn}(x', y') = \sin\left(\frac{m\pi x'}{L_x}\right) \sin\left(\frac{n\pi y'}{L_y}\right) \quad (63)$$

so

$$\begin{aligned} \frac{1}{c_t^2} \frac{\partial^2 A_{mn}(t)}{\partial t^2} + \left(\left(\frac{m\pi}{L_x} \right)^2 + \left(\frac{n\pi}{L_y} \right)^2 \right) A_{mn}(t) \\ = \frac{4}{m_a c_t^2 L_x L_y} \int_0^{L_x} \int_0^{L_y} p(x', y', t) \Phi_{mn}(x', y') dx' dy' \end{aligned} \quad (64)$$

Now if the displacement is stationary for $t < 0$ the Laplace transform can be taken of this equation and solve for $A_{mn}(t)$ as

$$\begin{aligned} A_{mn}(t) \\ = L^{-1} \left[\frac{4}{m_a c_t^2 L_x L_y \left(\frac{s^2}{c_t^2} + \left(\frac{m\pi}{L_x} \right)^2 + \left(\frac{n\pi}{L_y} \right)^2 \right)} \int_0^{L_x} \int_0^{L_y} L[p(x', y', t)] \Phi_{mn}(x', y') dx' dy' \right] \end{aligned} \quad (65)$$

Where $L[]$ and $L^{-1}[]$ represent a Laplace transform and it's inverse.

For this problem the pressure can be split into two parts,

$p(x', y', t) = f(t)g^{(1)}(x', y') + \partial f / \partial t (g^{(2)}(x', y'))$ and so we find that

$$A_{mn}^{(i)}(t) = \frac{G_{mn}^{(i)} f_{mn}^{(i)}(t)}{m_a} \quad (66)$$

$$f_{mn}^{(i)}(t) = L^{-1} \left[\frac{L[f^{(i)}(t)]}{(s^2 + \omega_{mn}^2)} \right] \quad (67)$$

Where $G_{mn}^{(i)} = (4/(L_x L_y)) \int_0^{L_x} \int_0^{L_y} g^{(i)}(x', y') \Phi_{mn}(x', y') dx' dy'$ and

$$\omega_{mn}^2 = (m\pi c_t/L_x)^2 + (n\pi c_t/L_y)^2$$

From the definition of the Wagner function

$$f^{(1)}(t) = 1 - ae^{-\alpha t} - be^{-\beta t} \quad (68)$$

Where $a=0.165, b=0.335, \alpha=0.0455, \beta=0.3$. And so

$$L[f^{(1)}(t)] = \frac{1}{s} - \frac{a}{s + \alpha} - \frac{b}{s + \beta} \quad (69)$$

and

$$f_{mn}^{(1)}(t) = \left(\frac{1 - \cos(\omega_{mn}t)}{\omega_{mn}^2} - a \left(\frac{e^{-\alpha t} - \left(\frac{\alpha}{\omega_{mn}} \right) \sin(\omega_{mn}t) - \cos(\omega_{mn}t)}{\omega_{mn}^2 + \alpha^2} \right) \right. \\ \left. - b \left(\frac{e^{-\beta t} - \left(\frac{\beta}{\omega_{mn}} \right) \sin(\omega_{mn}t) - \cos(\omega_{mn}t)}{\omega_{mn}^2 + \beta^2} \right) \right) \quad (70)$$

A similar expression is obtained for $f_{mn}^{(2)}(t)$ since $f^{(2)}(t) = \partial f^{(1)} / \partial t$

$$L[f^{(2)}(t)] = 1 - \frac{as}{s + \alpha} - \frac{bs}{s + \beta} \quad (71)$$

and

$$f_{mn}^{(2)}(t) = \left(\frac{\sin(\omega_{mn}t)}{\omega_{mn}} - a \left(\frac{\alpha e^{-\alpha t} - \alpha \cos(\omega_{mn}t) - \omega_{mn} \sin(\omega_{mn}t)}{\omega_{mn}^2 + \alpha^2} \right) \right. \\ \left. - b \left(\frac{\beta e^{-\beta t} - \beta \cos(\omega_{mn}t) - \omega_{mn} \sin(\omega_{mn}t)}{\omega_{mn}^2 + \beta^2} \right) \right) \quad (72)$$

$G_{mn}^{(i)}$ is defined as

$$G_{mn}^{(i)} = \left[\frac{4}{L_x L_y} \int_0^{L_x} \int_0^{L_y} g^{(i)}(x', y') \Phi_{mn}(x', y') dx' dy' \right] \quad (73)$$

For pulse type (1)

$$g^{(1)}(x', y') = \text{Im} \left(\frac{1}{x' - x'_c - x_o + ih} \right) = - \frac{h}{((x' - x'_c - x_o)^2 + h^2)}$$

And

$$(74)$$

$$G_{mn}^{(1)} = \left[\frac{4}{L_x L_y} \int_0^{L_x} \int_0^{L_y} \frac{h \sin\left(\frac{m\pi x'}{L_x}\right) \sin\left(\frac{n\pi y'}{L_y}\right)}{((x' - x'_c - x_o)^2 + h^2)} dx' dy' \right] \quad (75)$$

Where h is the distance of the wall from the airfoil. This gives

$$\begin{aligned} G_{mn}^{(1)} &= \left[\frac{4}{L_x L_y} \int_0^{L_x} \int_0^{L_y} \frac{h \sin\left(\frac{m\pi x'}{L_x}\right) \sin\left(\frac{n\pi y'}{L_y}\right)}{((x' - x'_c - x_o)^2 + h^2)} dx' dy' \right] \\ &= \frac{4h}{L_x} \left(\frac{1 - (-1)^n}{n\pi} \right) \int_{-x'_c - x_o}^{L_x - x'_c - x_o} \frac{\sin\left(\frac{m\pi(\gamma + x'_c + x_o)}{L_x}\right)}{(\gamma^2 + h^2)} d\gamma \end{aligned} \quad (76)$$

If $x_c \sim L_x/2 \gg l$ this integral is approximated as

$$\begin{aligned} G_{mn}^{(1)} &= \frac{4h}{L_x} \left(\frac{1 - (-1)^n}{n\pi} \right) \int_{-\infty}^{\infty} \frac{\sin\left(\frac{m\pi(\gamma + x'_c + x_o)}{L_x}\right)}{(\gamma^2 + h^2)} d\gamma \\ &= \frac{4h}{L_x} \left(\frac{1 - (-1)^n}{n\pi} \right) \int_{-\infty}^{\infty} \frac{\exp\left(\frac{im\pi(\gamma + x'_c + x_o)}{L_x}\right) - \exp\left(\frac{-im\pi(\gamma + x'_c + x_o)}{L_x}\right)}{2i(\gamma^2 + h^2)} d\gamma \\ &= \frac{4h}{L_x} \left(\frac{1 - (-1)^n}{n\pi} \right) \frac{\exp\left(\frac{im\pi(x'_c + x_o)}{L_x}\right) - \exp\left(\frac{-im\pi(x'_c + x_o)}{L_x}\right)}{4ih} e^{-\frac{m\pi h}{L_x}} \\ &= \frac{2}{L_x} \left(\frac{1 - (-1)^n}{n\pi} \right) \sin\left(\frac{m\pi(x'_c + x_o)}{L_x}\right) e^{-\frac{m\pi h}{L_x}} \end{aligned} \quad (77)$$

For pulse type (2)

$$g^{(2)}(x', y') = \text{Im}(\ln(z - x_o) - \ln(z)) \quad (78)$$

And note that

$$\frac{\partial g^{(2)}(x', y')}{\partial x'} = \text{Im} \left(\frac{1}{x' - x'_c - x_o + ih} - \frac{1}{x' - x'_c + ih} \right) \quad (79)$$

Continuing, integrating by parts gives

$$\begin{aligned} G_{mn}^{(2)} &= \frac{4}{L_x} \left(\frac{1 - (-1)^n}{n\pi} \right) \int_{-\infty}^{\infty} \sin \left(\frac{m\pi(\gamma + x'_c + x_o)}{L_x} \right) g^{(2)}(x', 0) d\gamma \\ &= \frac{4}{m\pi} \left(\frac{1 - (-1)^n}{n\pi} \right) \int_{-\infty}^{\infty} \cos \left(\frac{m\pi(\gamma + x'_c + x_o)}{L_x} \right) \frac{\partial g^{(2)}(x', 0)}{\partial x'} d\gamma \\ &= \frac{2h}{m\pi} \left(\frac{1 - (-1)^n}{n\pi} \right) \left(\cos \left(\frac{m\pi(x'_c + x_o)}{L_x} \right) - \cos \left(\frac{m\pi(x'_c)}{L_x} \right) \right) e^{-\frac{m\pi h}{L_x}} \end{aligned} \quad (80)$$

4.2 Sheet Vortex Model and Kevlar Membrane Results

The response of a Kevlar membrane due to a step change in angle of attack described by the Wagner's function is shown in figure 27. The tension of the membrane is 50 N/m and the flow speed is 30 m/s. The nonlinear term v_t^2 was not accounted for because it decays as $1/|z|^2$ and it is much smaller in magnitude. The response was calculated at the

airfoil's trailing edge and at a y location of h/c for a range of time. The displacement of the membrane due to the airfoil has a magnitude of 10 cm and the displacement due to the wake would be much smaller.

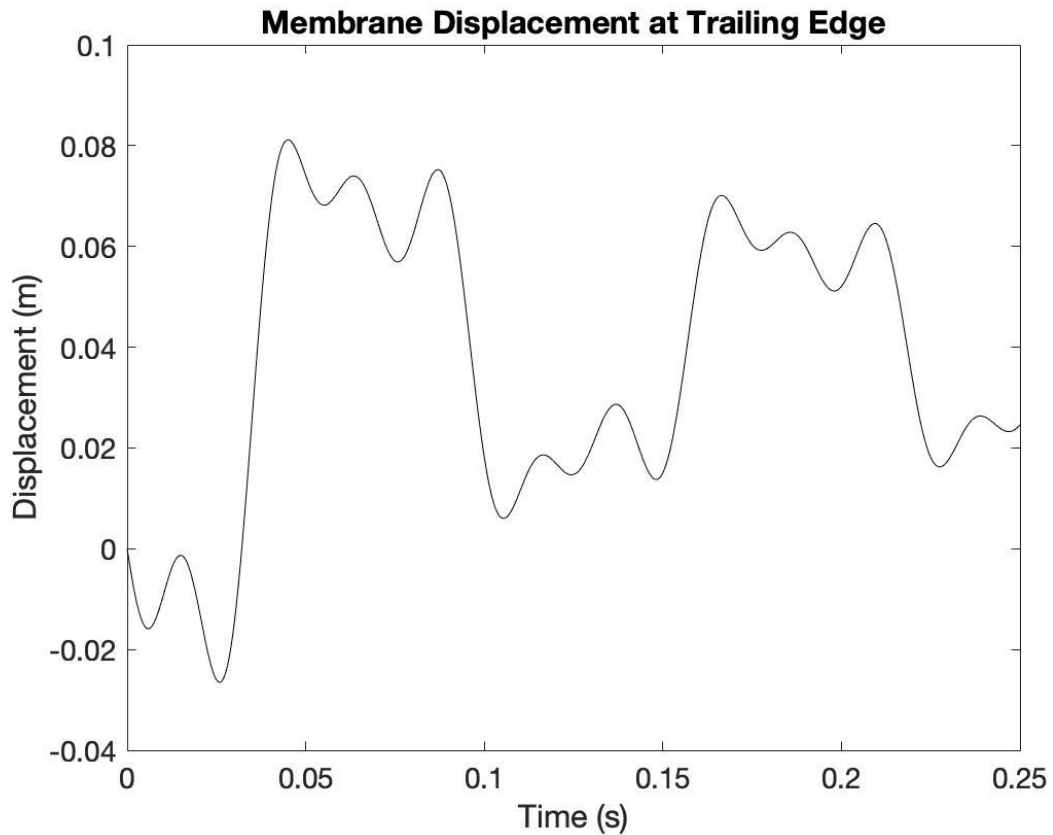


Figure 27: Kevlar Membrane Displacement at The Trailing Edge.

The tension of the membrane was varied to find the effects that tension has on the membrane response. The results shown in figure 28 are for three different tensions being 10, 50 and 2000 N/m and for a flow speed of 30 m/s. When the tension was reduced to 10 N/m the response of the membrane grew to 35 cm. When the tension was increased to

2000 N/m the response of the membrane reduced to .01 cm. The membrane response for a tension of 2000 N/m are similar to the results obtained by Brown et al. [4] in figure (3).

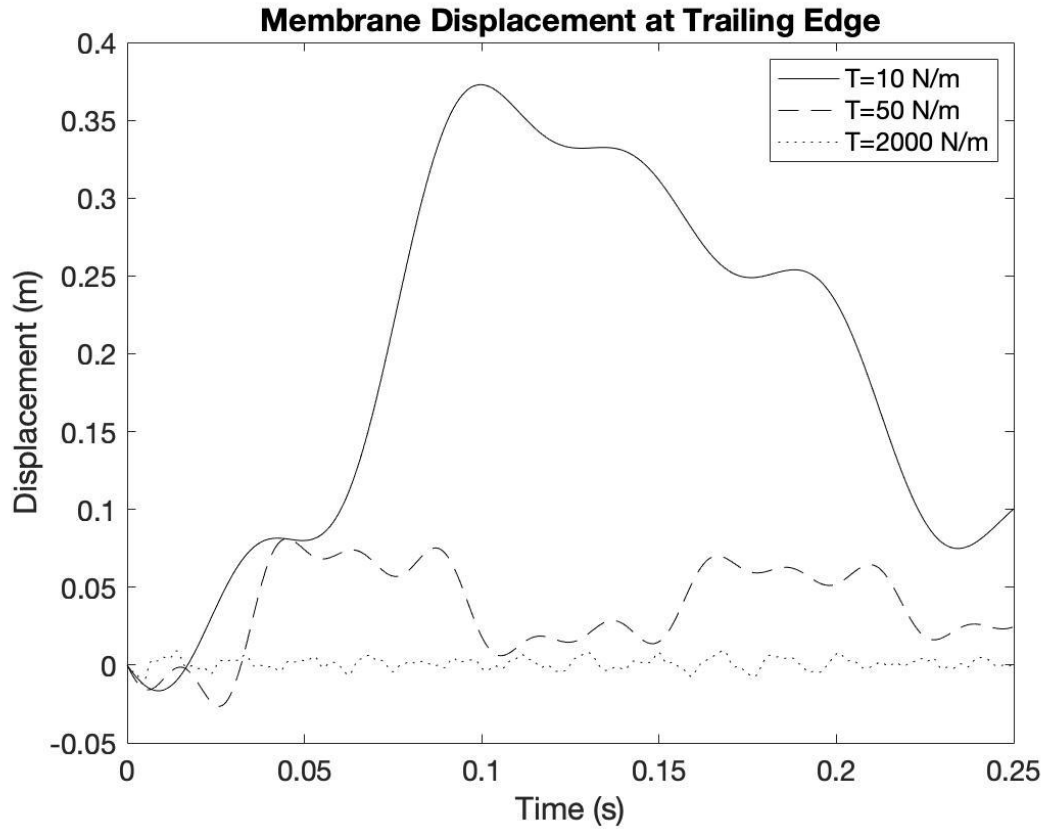


Figure 28: Kevlar Membrane Response at The Trailing Edge for Various Tension

The flow speed of the wind tunnel was varied to find the effects that flow speed has on the membrane response. The results shown in figure 29 are for three different flow speeds being 10, 30 and 50 m/s and for a tension of 30 N/m. When the flow speed was reduced to 10 m/s the response of the membrane peaked at 2 cm. When the flow speed was increased to 50 m/s the response of the membrane peaked around 20 cm. Tension and flow speed have an inverse relationship on the response of the membrane.

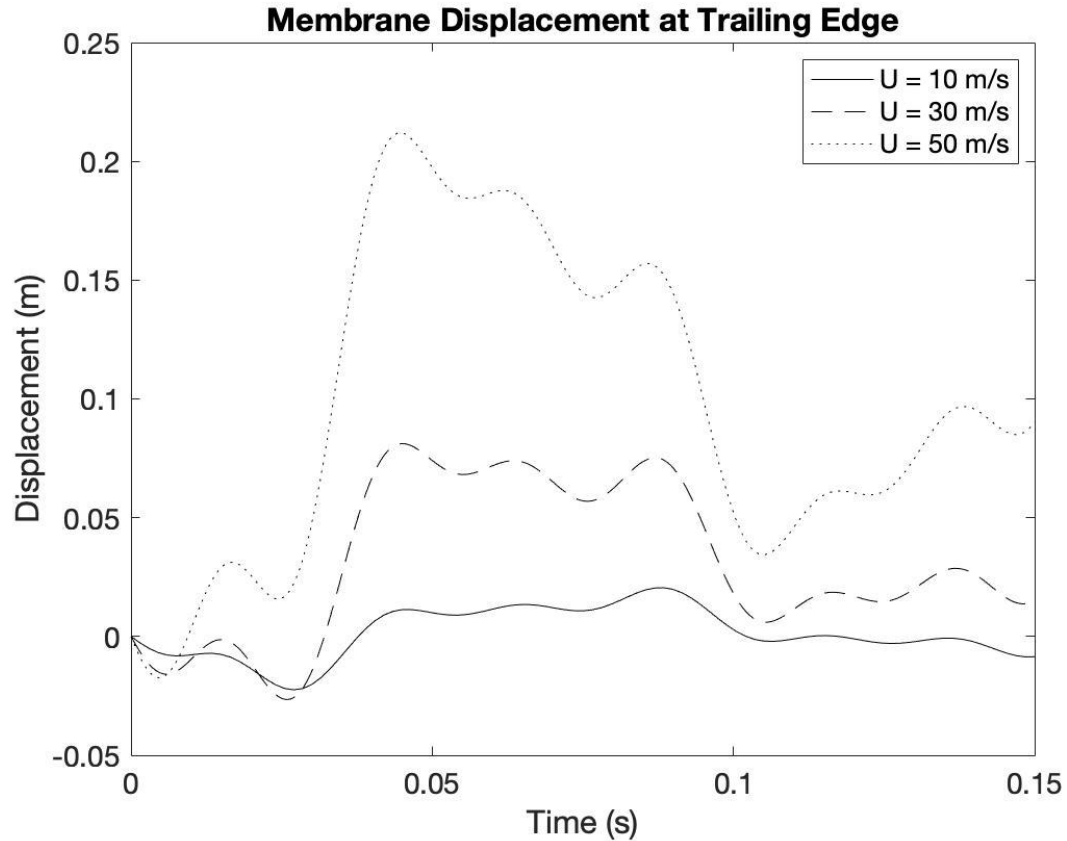


Figure 29: Kevlar Membrane Response at The Trailing Edge for Various Flow Speeds.

4.3 Sheet Vortex Model and Kevlar Membrane Conclusions

- The smallest and largest displacements were 0.01 cm and 35 cm respectively. The membrane response was influenced the most by changes in tension compared to changes in flow speed.
- The membrane response for a tension of 2000 N/m are similar to the results obtained by Brown et al. [4] in figure (3).
- Tension and flow speed have an inverse relationship on the response of the membrane. As the tension is increased the response is reduced and as the flow speed is increased the response is amplified.

- This Kevlar displacement method can measure the circulation around the airfoil which makes it an alternative method to force balance and unsteady lift measurements.
- The wake is only determined by the nonlinear term v_i^2 which decays as $1/|z|^2$ so it will be much smaller in magnitude. This means that the motion of the Kevlar is dominated by the effects of the airfoil and not the wake.
- Wall pressure transducers are required to measure the pressure perturbation of the wake.

Chapter 5: Discussion

5.1 Simple Vortex Model

The proposed measurement technique was used to analyze the startup vortex of an airfoil caused by a step change in angle of attack described by the Wagner's function. Potential flow theory was used to model the airfoil as a simple vortex and the shed vortex as an equal and opposite vortex. The impervious boundary condition for the 2 test section walls were approximated with a summation of 98 image vortices for each vortex, 49 above and 49 below. The images vortices reduced the velocity normal to the wall to $\sim 10^{-4}$ and this was sufficiently small. Since potential flow theory requires an ideal flow approximation, viscous flow effects were neglected such as flow separation and boundaries layers. This means that the flow used in the analysis of this thesis is different from the flow during a physical experiment. During real world wind tunnel experiments, a turbulent boundary layer forms along the wall that emits rapid pressure fluctuations. An empirical interpolation formula, created by Goody, was used to estimate the wall pressure frequency spectrum of the wall turbulent boundary layer so that rms pressure at the wall could be approximated [1]. The estimated C_{prms} was found to be of the order of 10^{-2} and is relatively small compared to the C_p values that peak around 2.2.

The time history of the transient flow for a startup vortex of an airfoil caused by a step change in angle of attack was divided into 2 regimes, time before and time after the critical time. Bernoulli's equation for unsteady potential flows was used to derive the

governing equations for the pressure along the wall for both these flow regimes. An important part of this model was to accurately estimate the critical time of vortex separation. The critical time was approximated to be 10 seconds by determining the time it takes for the Wagner function to reach 92 percent of its true value. This could be a possible source of error and future real world experiments should include measuring the critical time of vortex separation. The Wagner function was also used to model the growth of the strength of the startup vortex as a function of time for time less than the critical time.

After the critical time is reached, the startup vortex begins to separate from the trailing edge and both its strength and position could be a function of time. It was assumed that the convection speed grows linearly with time and the acceleration time is half of the convection period. The convection period has a large effect on the wall pressure signal and accurately estimating its value is another important part of this analysis. Varying the convection period resulted in signals with different shapes and maxima values. Unfortunately, this value is unknown, and it must be measured during physical wind tunnel experiments. This could be a possible source of error. Furthermore, in this analysis the strength of the shed vortex was held constant while it accelerated downstream. In reality, its strength could change during acceleration. This was not accounted for and could be another source of error.

The time varying pressure signal using a convection period of 50 seconds was obtained for multiple locations along the wind tunnel wall. The results for a transducer imbedded into the wind tunnel wall at the mid chord point shows a positive pressure wave with a peak at 1.2 that converges to a value around 1. The discontinuity that occurs

during critical time is due to the shed vortex separating from the trailing edge as it begins to accelerate downstream due to an instantaneous change in angle of attack. The signal is 100 times greater than the estimated background noise from the turbulent boundary layer along the wall. This signal has a non-zero starting point that would make frequency analysis difficult, so this is not an ideal location for a transducer.

The results for a transducer imbedded into the wind tunnel wall located 1 chord length downstream shows that the signal starts to reverse because here the signal is comprised of the airfoil signature and the wake signature. There is another discontinuity that occurs at the critical time. This signal starts at zero and this position is a possible location to place transducer, but the signal is in the process of reversing and is dominated by the airfoil signature.

The results for a transducer imbedded into the wind tunnel wall located 3 chord length downstream shows a signal that is entirely negative, starts at zero and converges to a value of -0.2. This is because the signal contains the whole pressure wave of the wake and the airfoil signature is minimal. This is an idea location to place a transducer to measure the wake signature.

Gaussian noise with a magnitude equal to the estimate rms pressure of the wall turbulent boundary layer was added to the signal. This was done to simulate noise that may be present in physical wind tunnel measurements. Spectral analysis of the noisy signal revealed that the pressure wave induced by the startup vortex occurs at a nondimensional frequency around 0.1 and broad band noise across all frequencies. At digital band pass filter was able to remove most of the noise even at 10 time the estimate noise levels.

The discontinuity in the pressure time signal is an error that reduces the accuracy of the pressure estimates. A more accurate model is explored in the next section.

5.2 Vortex Sheet Model and Kevlar Wall Response

This model used a vortex sheet to describe the wake of the airfoil. This model also used potential flow theory, so the flow is ideal. The displacement of the airfoil in the y direction is ignored and this is valid for thin airfoil theory. The effect of the wind tunnels walls has been investigated in detail for the simple vortex model but in this section the effects have been omitted. It was found that the contribution from the wake is determined by the nonlinear term v_t^2 which decays as $1/|z|^2$ so it will be much smaller in magnitude. So, the analysis for the Kevlar wall response only considered the contribution of the linear term, or the circulation around the airfoil and not its wake. This model led to a solution for the response of a Kevlar wall through Laplace transforms which the first model could not. The Kevlar membrane response showed that it is possible to measure the unsteady circulation and therefore the unsteady lift of an airfoil, but the wake signature is too small in magnitude to measure this way.

The effects of flow speed and membrane tension on the membrane response were explored. It was found that flow speed and membrane tension have an inverse relationship. At higher flow speeds the membrane had a larger displacement while at larger tensions the membrane had smaller displacement. This makes sense intuitively. Finally, the membrane displacement for a tension of 2000 N/m is similar to those of Brown et al. [4].

Chapter 6: Conclusion

6.1 Conclusion

- Two models of an airfoil were created based on thin airfoil theory. The simple vortex model was the most basic way to represent the airfoil and its wake. The airfoil and its wake based on step change in angle of attack were modeled according to Kelvins theorem as two equal and opposite vortices. The pressure signal produced by this model was comprised of the airfoil vortex signature and the wake vortex signature. It was determined that at 3 chord lengths or more downstream the wake signature is dominate and can be obtained. The pressure signal from this model had a discontinuity at the critical time due to the instantaneous change in angle of attack described by the Wagner function. This is unrealistic and adds inaccuracy to the results.
- The critical time at which the starting vortex of an airfoil separates and begins to convect downstream was determined by the Wagner's function at 92 percent of its true value. Furthermore, the unsteady circulation and lift were determined by the Wagner function which created a discontinuity in the pressure time signal. This is an unrealistic result.
- The critical time should be investigated more accurately via physical wind tunnel experiments to obtain a more realistic model.
- The acceleration of the starting vortex as it begins to convect downstream was assumed to grown linearly with time and to reach a mean value at half of the

period of acceleration. The convection acceleration period has a direct effect on the pressure signature along the wall and its true value is only determined by physical wind tunnel experiments. Since the acceleration period is unknown, 6 different values were explored and a period of $T=50$ was chosen for the simple vortex model.

- Goody's model of wall pressure frequency spectrum for a turbulent boundary layer was used to estimate the background noise. The rms estimates were much smaller than the desired pressure wave from the startup vortex of the airfoil. A digital bandpass filter was able to remove noise from the signal at 10 times the estimated background noise. Therefore, the signal induced by the airfoil is sufficiently large enough to be obtained by a wall mounted pressure transducer.
- The second model represents the airfoil as a vortex and the wake as a vortex sheet. This model was also based on a step change in angle of attack described by the Wagner function so the signal also had a discontinuity at the critical time. This model led to a solution for the response of a Kevlar wall through Laplace transforms which the first model could not. The accuracy of this model can be improved by considering the wake term and using a different forcing function to describe the rate of change in angle of attack.
- The wake is determined by the nonlinear term v_t^2 which decays as $1/|z|^2$ so it will be much smaller in magnitude. This means that the motion of the Kevlar is dominated by the effects of the circulation about the airfoil and not the wake.

- The smallest and largest displacements were 0.01 cm and 35 cm respectively and they were caused by a change in membrane tension. The membrane response was influenced the most by changes in tension compared to changes in flow speed.
- The membrane displacement for a tension of 2000 N/m is similar to those of Brown et al. [4].
- The Kevlar displacement method can measure the unsteady circulation and the unsteady lift of an airfoil. This serves as a noninvasive method for invasive force balance measurements for unsteady lift. This would allow for better acoustic measurements as there would be no noise produced by the flow around equipment placed into the flow.
- The wake signature is dominated by the nonlinear term v_i^2 so wall pressure transducers are required to measure the pressure perturbation of the wake.
- The pressure history of a wake can be obtained with a 2 dimensional array of wall mounted pressure transducers, providing a promising noninvasive method of measuring wall pressures of a transient flow.

6.2 Recommendations

- A new model of the airfoil and its wake can be created using conformal mapping that could describe the velocities of the flow more accurately.
- Physical wind tunnel experiments should be conducted to better estimate the critical time of vortex separation and the convection acceleration period. Physical experiments will also determine the accuracy of the proposed measurement method relative to current methods.

- Investigate different forcing functions to vary the rate of change of angle of attack such as a ramp function or a Gaussian function.
- The wake signature should be investigated by considering the contribution of the nonlinear term of the Bernoulli's equation. Furthermore, the rate of change of angle of attack should be varied according to other functions such as a ramp and a Gaussian forcing function.

Chapter 7: Appendix

7.1 Additional Information on Kenneth Brown's Work

Determining a load from deflection, for instance calculating the pressure along a Kevlar wall from its displacement, creates an inverse problem. The governing equilibrium equations in structural mechanics relates the derivative of the displacement field to loading applied to the opposite side [4]. Taking a derivative of the displacement field dramatically increases any errors that are contained in the data set. This means that a very small error in a sensor's measurement may be magnified to a significant amount that could discredit the final results. According to Brown et al.'s [4], the magnified error due to differentiation can be mitigated by various regularization techniques. Brown et al.'s [4] approach used a finite-element study and then treated the displacement input by projecting the displacement measurements onto a coarse grid using C^2 continuous triangulation-based bicubic interpolation. Then the data set was regularized by least-squares projecting the data onto basis functions [4]. Additionally, a series of basis functions were used so that the accuracy of the solution is determined by the number of terms kept in the series [4]. Brown et al.'s [4] utilized the following global polynomial for the basis function.

$$u = \sum_{i=0}^a \sum_{j=0}^b l_{ij} x^i y^j \quad v = \sum_{i=0}^c \sum_{j=0}^d m_{ij} x^i y^j \quad w = \sum_{i=0}^e \sum_{j=0}^f n_{ij} x^i y^j \quad (81)$$

Least squared regression of the data was used to obtain the coefficients l_{ij} , m_{ij} , n_{ij} , x and y were the distance from the origin in the respective directions and a sensitivity study was used to decide the values for a , b , c , d , e , and f [4].

The Kevlar used in this study consisted of woven Kevlar fabrics that ran in perpendicular directions to form a sheet. The ratio of the length of the periodic micro-scale to the length scale of the Kevlar sheet was used to determine if the sheet could be assumed as a continuous material [4]. With 13 pores per centimeter and an overall length of 1.85 meter, the fabric was assumed to be continuous, and the orthotropic elastic lamina was chosen as the continuum model [4]. The 2 directions of the woven fibers were modeled by two perpendicular plans of elasticity, the material was approximated as linear since the strains are sufficiently small and the small thickness of the material allowed for that twisting and bending stresses to be assumed zero. Brown et al.'s [4] considered a differential membrane element to derive the following governing equations for the strain displacement relationship.

$$\varepsilon_x = \frac{\partial u}{\partial x} + \frac{1}{2} \left(\frac{\partial w}{\partial x} \right)^2 \quad \varepsilon_y = \frac{\partial v}{\partial y} + \frac{1}{2} \left(\frac{\partial w}{\partial y} \right)^2 \quad \gamma_{xy} = \frac{\partial u}{\partial y} + \frac{\partial v}{\partial x} + \frac{\partial w}{\partial x} \frac{\partial w}{\partial y} \quad (82)$$

The relationship between stress and strain for an orthotropic elastic membrane are as follows where T is the tension, E is the elastic moduli, ν is Poisson's ratio, G is the shear modulus, H is the fabric thickness and where the ε subscript indicates the strain induced tension [4].

$$T_{x,\varepsilon} = \frac{E_x H}{1 - v_{xy} v_{yx}} (\varepsilon_x + v_{yx} \varepsilon_y) \quad T_{y,\varepsilon} = \frac{E_y H}{1 - v_{xy} v_{yx}} (\varepsilon_y + v_{xy} \varepsilon_x) \quad T_{xy,\varepsilon} = GH \gamma_{xy}$$

(83)

Chapter 8: References

- [1] S. Glegg and W. Devenport, *Aeroacoustics of Low Mach Number Flows: Fundamentals, Analysis, and Measurement*, London: Joe Hayton, 2017.
- [2] C. J. Bahr and F. V. Hutcheson, "Unsteady Propagation and Mean Corrections in Open-Jet and Kevlar® Wind Tunnels," *AIAA JOURNAL*, vol. 59, no. 11, 2021.
- [3] M. Szoke, S. A. Glegg and W. J. Devenport, "Investigating the Aeroacoustic Properties of Kevlar Fabrics," *AIAA JOURNAL*, Vols. 2021-2255, 2021.
- [4] Y. Mayer, B. Zang and M. Azarpeyvand, "Aeroacoustic investigation of an oscillating airfoil in the pre- and post-stall regime," *Aerospace Science and Technology*, vol. 103, p. 105880, 2020.
- [5] J. B. Barlow, J. William H. Rae and A. Pope, *Low-Speed Wind Tunnel Testing*, Third ed., New York: John Wiley & Sons, Inc., 1999.
- [6] "Reynolds Number," 12 July 2014. [Online]. Available: <https://www.grc.nasa.gov/www/BGH/reynolds.html>. [Accessed 15 March 2021].
- [7] K. Brown, J. Brown, M. Patil and W. Devenport, "Inverse measurement of wall pressure field in flexible-wall wind tunnels using global wall deformation data," *Experiments in Fluids*, vol. 59, no. 25, 2018.
- [8] K. A. Brown, "A Study of Aerodynamics in Kevlar-Wall Test Sections," Blacksburg, 2014.
- [9] J. N. Newman, *Marine Hydrodynamics 40th Anniversary Edition*, Massachusetts: The MIT Press, 2017.
- [10] "Shed Vortex," 5 May 2015. [Online]. Available: <https://www.grc.nasa.gov/www/k-12/airplane/shed.html>. [Accessed 2020].
- [11] J. Liburdy, "Intermediate Fluid Mechanics," [Online]. Available: <https://open.oregonstate.edu/intermediate-fluid-mechanics/chapter/potential-flows/>. [Accessed 3 22 2021].

- [12] R. Fitzpatrick, "Method of Images," 31 03 2016. [Online]. Available: <http://farside.ph.utexas.edu/teaching/336L/Fluidhtml/node86.html>. [Accessed 2021].
- [13] G. Grasso, P. Jaiswal, H. Wu, S. Moreau and M. Roger, "Analytical models of the wall-pressure spectrum under a turbulent boundary layer with adverse pressure gradient," *Journal of Fluid Mechanics*, vol. 877, pp. 1007-1062, 2019.
- [14] W. J. Devenport, R. A. Burdisso, A. Borgoltz, P. A. Ravetta, M. F. Barone, K. A. Brown and M. A. Morton, "The Kevlar-walled Anechoic Wind Tunnel," *Journal of Sound and Vibration*, vol. 3971, no. 3991, 2013.
- [15] R. L. Bisplinghoff and H. Ashley, *Principles of Aeroelasticity*, New York: Dover Publications, INC, 1975.